PHYSICAL REVIEW D **75,** 024005 (2007)

"Kludge" gravitational waveforms for a test-body orbiting a Kerr black hole

Stanislav Babak*
[1]*Max-Planck-Institut fuer Gravitationsphysik, Albert-Einstein-Institut, Am Muchlenberg 1, D-14476 Golm bei Potsdam, Germany*

Hua Fang†
[2]*Theoretical Astrophysics, California Institute of Technology, Pasadena, California 91125, USA*

Jonathan R. Gair‡
[3]*Institute of Astronomy, Madingley Road, Cambridge, CB3 0HA, UK*

Kostas Glampedakis§
[4]*School of Mathematics, University of Southampton, Southampton SO17 1BJ, UK*

Scott A. Hughes‖
[5]*Department of Physics and MIT Kavli Institute, Massachusetts Institute of Technology, 77 Massachusetts Avenue, Cambridge, Massachusetts 02139, USA*
(Received 4 July 2006; published 4 January 2007)

One of the most exciting potential sources of gravitational waves for low-frequency, space-based gravitational wave (GW) detectors such as the proposed Laser Interferometer Space Antenna (LISA) is the inspiral of compact objects into massive black holes in the centers of galaxies. The detection of waves from such "extreme mass ratio inspiral" systems (EMRIs) and extraction of information from those waves require template waveforms. The systems' extreme mass ratio means that their waveforms can be determined accurately using black hole perturbation theory. Such calculations are computationally very expensive. There is a pressing need for families of approximate waveforms that may be generated cheaply and quickly but which still capture the main features of true waveforms. In this paper, we introduce a family of such kludge waveforms and describe ways to generate them. Different kinds of kludges have already been used to scope out data analysis issues for LISA. The models we study here are based on computing a particle's inspiral trajectory in Boyer-Lindquist coordinates, and subsequent identification of these coordinates with flat-space spherical polar coordinates. A gravitational waveform may then be computed from the multipole moments of the trajectory in these coordinates, using well-known solutions of the linearised gravitational perturbation equations in flat space time. We compute waveforms using a standard slow-motion quadrupole formula, a quadrupole/octupole formula, and a fast-motion, weak-field formula originally developed by Press. We assess these approximations by comparing to accurate waveforms obtained by solving the Teukolsky equation in the adiabatic limit (neglecting GW back-reaction). We find that the kludge waveforms do extremely well at approximating the true gravitational waveform, having overlaps with the Teukolsky waveforms of 95% or higher over most of the parameter space for which comparisons can currently be made. Indeed, we find these kludges to be of such high quality (despite their ease of calculation) that it is possible they may play some role in the final search of LISA data for EMRIs.

DOI: 10.1103/PhysRevD.75.024005 PACS numbers: 04.30.Db, 04.80.Nn, 04.25.Nx

I. INTRODUCTION-MOTIVATION

The proposed Laser Interferometer Space Antenna (LISA) [1], is expected to provide a variety of high-precision gravitational wave (GW) measurements. One of the most interesting targets for this space-based detector are the GWs generated by stellar-mass compact objects inspiralling into (super)massive black holes [(S)MBHs[1]]. Accumulated astrometric observations provide strong support in favor of the existence of a "dark" compact object in the core of every galaxy (for which the central parsec region can be resolved) [2]. With masses ranging between

*Electronic address: stba@aei.mpg.de
†Electronic address: hua@tapir.caltech.edu
‡Electronic address: jgair@ast.cam.ac.uk
§Electronic address: kg1@maths.soton.ac.uk
‖Electronic address: sahughes@mit.edu

[1]LISA's sensitivity is primarily to events involving black holes on the low end of the mass spectrum seen in many galaxies—around 10^5 to (a few) $\times 10^7 M_\odot$. We emphasize this point because the name "supermassive black hole" is often taken to refer to a hole with mass in the range 10^7–$10^9 M_\odot$. GW events from such black holes will typically be at frequencies too low for LISA's sensitivity.

10^6–$10^9 M_\odot$ these objects are believed to be massive Kerr black holes [3]. It is also believed that these holes are the ''quiet'' remnants of an older quasar population [4].

Multibody interactions in the ''cusp'' stellar population surrounding these SMBHs can put stellar-mass compact objects onto orbits that come close to the central black hole. If the object passes sufficiently close to the (S)MBH, it may be captured and subsequently spiral in by the emission of GWs [5–7]. Initially, the captured bodies are expected to be on ''generic'' orbits, i.e., eccentric (with eccentricity $e \approx 1$) and inclined with respect to the central black hole's equatorial plane [5,8]. These orbits evolve adiabatically due to GW emission, decreasing in eccentricity and periastron while the inclination of the orbit remains approximately constant, but increases slightly (see [9–11] for an approximate description of the full inspiral).

For central black hole masses in the range $10^5 M_\odot \lesssim M \lesssim 10^7 M_\odot$, the GWs emitted during the inspiral will be at frequencies close to the floor of the LISA noise curve (~ 3 mHz). LISA will detect the bursts of radiation emitted near periapse throughout the inspiral, but these will not be individually resolvable [12] unless they occur in our Galaxy [13]. However, during the last few years of inspiral, when the small object is orbiting deep inside the SMBH's gravitational field, GWs are radiated continuously in the LISA band. During this phase, the residual eccentricity is typically at $e \lesssim 0.4$ [9,10] and the orbital motion will exhibit extreme versions of relativistic effects (e.g., periastron and Lense-Thirring precession). As a consequence, the resulting GW signal will be strongly ''colored'' by these effects and will take a complicated form [14,15]. By complicating the waveform, these strong-field effects potentially make data analysis difficult; but, they also encode a great deal of information about the strong field nature of the spacetime. By accurately measuring all of these effects, it is expected that we will be able to ''map'' the spacetime of the black hole [16], probing its multipolar structure and verifying that it obeys the constraints that general relativity imposes on black hole solutions [17,18].

The expected amplitude of the signal from these extreme-mass-ratio inspirals (EMRIs) is about an order of magnitude below LISA's projected instrumental noise and, at low frequencies ($\lesssim 2$ mHz), is several orders of magnitude below ''confusion noise'' produced by unresolved Galactic binaries [19]. However, the signals will be observed for $\sim 10^5$ waveform cycles, and matched filtering will therefore allow detection of these signals with high signal-to-noise ratio (SNR) out to a redshift $z \sim 1$ [20]. Preliminary estimates suggest LISA could see as many as $\sim 10^3$ EMRI events during its lifetime [7,20], using a suitable ''semicoherent'' search algorithm and provided that confusion noise can be efficiently reduced in the real data.

Matched filtering algorithms require the correlation of the detector's output data stream with a bank of waveform templates which describe the real signal with sufficient accuracy, covering the whole parameter space. The fact that we are dealing with a binary system of extreme mass ratio $\mu/M \ll 1$ means that the gravitational waveform may be obtained accurately using black hole perturbation theory. The extreme mass ratio also guarantees that the orbital parameters evolve adiabatically under radiation reaction; i.e., they evolve on a much longer time scale than the orbital periods. This implies that within the radiation-reaction time scale, the inspiral waveform can be approximated by ''snapshot'' waveforms—waveforms calculated by assuming that the small object is moving along a geodesic, neglecting backreaction for that short stretch of time. These snapshots are constructed using the Teukolsky equation [21], an equation that describes the first-order change to the curvature tensor of a black hole due to some perturbing source. Accurate Teukolsky-based (TB) snapshot waveforms have been calculated for inclined-circular orbits [14], equatorial-eccentric orbits [15,22,23] and most recently, for a certain number of generic (inclined-eccentric) orbits [24]. The reader can find recent reviews on the modeling of EMRI waveforms and orbital dynamics in Refs. [11,25].

TB waveforms are computationally expensive to generate as they require the numerical integration of the Teukolsky equation and summation over a large number of multipole modes. In this sense, these waveforms are not ''user-friendly'', especially when it comes to realistic data analysis calculations where one has to handle a bank which contains $\sim 10^{12}$ of these waveforms [20]. Moreover, the Teukolsky formalism does not provide any information on ''conservative'' self-interaction effects. To compute these, one must use a self-force formalism. This approach is still under development and is very likely to be even more computationally expensive when it is completed (see [26] for a recent review).

These difficulties have led to a need for the construction of approximate families of waveforms that capture the main features of the true signals, but which can be generated quickly in large numbers. Such approximate waveforms are already being used for scoping out data analysis algorithms for the detection of EMRIs in LISA data [20], and may ultimately play some role as fiducial detection templates in the final data analysis. One possible approach is to construct post-Newtonian (PN) waveforms, which have the advantage of being analytic and therefore very easy to generate. Post-Newtonian EMRI waveforms have been computed in the Schwarzschild spacetime for both quasicircular [27] and eccentric orbits [28], and in the spacetime outside a slowly rotating Kerr black hole for quasicircular orbits [29].

Recently another class of approximate waveforms have become available, based on various ''kludge'' approaches [30]. The basic idea of the kludges is to combine different prescriptions for the orbital evolution and waveform emis-

sion (not necessarily in a self-consistent way). An "analytic kludge" (AK) was developed by Barack and Cutler [31] (see also [32]). In their model, the small object is moving on a Keplerian orbit, amended to include the effects of pericenter precession, Lense-Thirring precession, and inspiral from radiation reaction. The emitted gravitational waveforms are described by the lowest-order quadrupole formula.

In this paper, we consider an alternative way to construct kludge waveforms. This approach is much less amenable to analytic calculation, so we called it the "numerical kludge" (NK). The first step of the NK is to produce an inspiral trajectory in "phase space"—the space defined by the constants (orbital energy, axial angular momentum, and "Carter constant") which specify orbits (up to initial conditions) [9,10]. The second step is to numerically integrate the Kerr geodesic equations along this inspiral trajectory and hence obtain the Boyer-Lindquist coordinates of the inspiralling object as a function of time [33]. The final step is to construct a gravitational waveform from this inspiral trajectory.

The approach to waveform construction that we take is to identify the Boyer-Lindquist coordinates of the source with spherical polar coordinates in flat-space. There are several different expressions available in the literature for the gravitational waveforms from orbits in flat space, and we apply these to our pseudo-flat-space trajectory to construct waveforms. Specifically, we look at the quadrupole formula [34], which is valid in the limit of weak-field (i.e., flat-space) and slow motion. We also examine the quadrupole-octupole formula of Bekenstein [35], as well as a formula derived by Press [36]. The Press formula is also a weak-field expression, but is not restricted to slow-motion or small sources, and contains radiation at orders higher than quadrupole and octupole.

The purpose of this paper to establish and delimit the accuracy and reliability of waveforms constructed in these various ways. We do this by comparing to TB waveforms. TB waveforms are currently the most accurate EMRI waveforms available. In most cases, TB waveforms represent the emission from geodesic orbits—we mostly do not include the radiative evolution of orbital parameters in this work. (With one exception: because complete TB inspirals exist for zero-eccentricity orbits [37], we compare to a full inspiral in this case.) We compare the various NK waveforms with TB waveforms using an overlap integral which weights the waveforms in frequency space by the expected LISA noise curve, and maximizes the overlap with respect to time offsets. This overlap is identical to the test used to evaluate the efficiency of model waveforms as detection templates.

We find that quadrupole-octupole NK waveforms are in remarkable agreement (overlaps $\gtrsim 0.95$) with TB waveforms for orbits with periastron $r_p \gtrsim 5M$. Most orbits in the final year of the inspiral satisfy this restriction which means that NK waveforms are quite accurate over a considerable portion of the inspiral parameter space. For orbits that come below that radius (mostly prograde orbits around rapidly spinning holes), the agreement rapidly degrades (although NK waveforms remain more accurate than post-Newtonian or AK waveforms). This is not surprising—for such orbits the full TB waveform receives significant contributions from higher multipoles and backscattering from the spacetime. These effects are *ab initio* absent in the NK prescription. Waveforms generated using the Press formula perform similarly well for $r_p \gtrsim 5M$, and slightly better than the quadrupole-octupole prescription for orbits where the contribution from higher harmonics is not negligible. The improvement in this relatively strong-field regime is only slight, however—we did not find any regime where the Press formula is a significant improvement on the quadrupole-octupole prescription. We conclude that NK waveforms can accurately reproduce true gravitational waveforms in a large part of parameter space; but, there is little gain from going beyond the quadrupole-octupole prescription.

We also calculate kludge radiation *fluxes* by combining the quadrupole energy flux formula with exact geodesic motion and averaging in time; such an analysis was done for Schwarzschild orbits in [38]. The resulting fluxes typically compare well to the best available PN formula in the weak field, but provide a somewhat better estimate of the energy and angular momentum fluxes (comparing to TB results) for strong-field orbits. These fluxes also allows us to assess by how much the approximations which go into the kludge construction are inconsistent. Since the inspiral trajectory and waveform construction are considered separately, kludge GWs carry a different amount of energy and angular momentum to infinity than the inspiralling particle loses (which is set by the formulas which determine the inspiral through orbital parameter space). It is important to bear this in mind when using kludge waveforms in computations, e.g., for estimating SNRs of LISA EMRI detections, and to have an estimate of the size of the inconsistency. Finally, we describe how the kludge waveforms may be improved by including some of the conservative self-force effects, which may have a significant imprint on true inspiral waveforms.

This paper is organised as follows. Section II provides a review of existing EMRI waveforms, paying special attention to the kludge semirelativistic waveforms. Details of how these waveforms can be generated are described. In Sec. III we discuss the overlap function between two waveforms, as this will be our main tool for comparison. Section IV contains the results from the comparison between kludge and Teukolsky-based waveforms and fluxes. In Sec. V a method is outlined for including the conservative parts of the self-force in our kludge scheme. Finally, we present a concluding discussion in Sec. VI. We shall use greek letters (μ, ν, etc.) to denote spacetime indices, and

Latin letters (i, j, etc.) to denote spatial indices (unless explicitly stated otherwise). Throughout the paper we adopt geometric units $G = c = 1$.

II. WAVEFORM INVENTORY

Presently, several types of EMRI waveforms are available. In broad terms, these waveforms fall into three categories: (i) those calculated numerically within the framework of black hole perturbation theory (Teukolsky-based, or TB waveforms), (ii) analytic waveforms which result from self-consistent PN expansions of the GW equations *and* orbital motion, and (iii) approximate semirelativistic waveforms, or ''kludges''. This third category is the focus of this paper.

Kludge waveforms are constructed by combining a flat-spacetime wave-emission formula with either a fully relativistic treatment of particle motion (resulting in the numerical kludge, or NK, waveforms), or some analytic approximation of this motion (leading to the analytic kludge, or AK, waveforms). We shall examine the construction of NK waveforms, comparing them to TB waveforms (the most accurate EMRI waveforms presently available). For completeness and background to this paper's discussions, we now briefly discuss each of the above waveform families.

A. Teukolsky-based numerical waveforms

The primary framework for black hole perturbation theory in a Kerr background is the Teukolsky formalism [21], which encapsulates all gravitational radiative degrees of freedom in a single ''master'' wave equation—the ''Teukolsky equation''—for the Weyl scalars ψ_0 and ψ_4. A key feature of this equation is that it admits separation of variables in the frequency domain, which effectively reduces it to a pair of ordinary differential equations. There are extensive results in the literature on solutions of the Teukolsky equation, starting from Press and Teukolsky [39], Detweiler [40] and Sasaki and Nakamura [41]. More recent work uses the Teukolsky-Sasaki-Nakamura formalism, see Refs. [11,25] for detailed discussions and references on the subject.

To date, the Teukolsky equation has been solved in the frequency domain for circular-inclined orbits [14], eccentric-equatorial orbits [15] and most recently for a handful of generic (eccentric-inclined) orbits [24]. We make use of the waveforms generated by these various authors in this paper to assess the quality of our NK waveforms. Recently, the Teukolsky equation has also been solved directly in the time domain [42,43]. Time-domain calculations have the great advantage of speed, since they avoid the need for Fourier decomposition and summation over all orbital frequency harmonics. However, these calculations are not yet mature enough to provide accurate waveforms from Kerr orbits, because of the difficulty of representing the various δ-functions appearing in the energy-momentum tensor of a point particle.

As a final remark, we should mention again that in all the above TB calculations (either in the frequency or the time domain) the motion of the small object is taken to be strictly geodesic. This is a reasonable first approximation since for an EMRI system the orbital evolution is adiabatic, i.e., over a time interval of several orbits the motion is geodesic to high precision. However, for longer stretches of time ($\sim M^2/\mu$) the effects of gravitational backreaction become significant and cannot be ignored anymore. Waveforms that take into account an evolving orbit (and the conservative self-interaction) require the computation of the gravitational self-force (see [44] for an up-to-date review and a full list of references). However, self-force waveforms are not yet available and are unlikely to be for the next few years. Moreover, it is very likely that self-force calculations will remain quite computationally intensive; as such, it is very likely that it will not be possible to generate self-force based waveforms in sufficient numbers to be used for LISA data analysis. It is therefore essential to investigate approximate, easy-to-use waveform models.

B. Analytic waveforms

Most available analytic waveforms are based on post-Newtonian expansions of the orbital dynamics and wave emission, an expansion that is of greatest relevance when the bodies are widely separated. These waveforms are typically constructed for a specific object or for restricted orbital motion. A significant amount of work has been done on modeling waveforms from two spinning bodies with comparable masses orbiting in precessing quasicircular orbits (a key GW source for both ground- and space-based detectors). Kidder [45] has investigated the effects of spin-spin and spin-orbital coupling on the waveform from inspiralling binaries. The most recent investigation of PN waveforms (and their application to data analysis) for spinning binary systems may be found in Refs. [46–48] (see also references therein). Another promising approach is described in [49], which is the first attempt to extend the ''effective-one-body'' method [50] to spinning compact objects. In parallel to modeling spinning binaries in quasicircular orbits, there has been significant progress in the construction of waveforms for eccentric, comparable mass binaries [51–53]. Presently, there are no post-Newtonian waveforms which include both eccentricity of the orbit and spins of the orbiting bodies.

Post-Newtonian models are ultimately not so useful for modeling EMRIs, since most of the GWs observable to LISA are generated from a strong-field region ($r \sim$ a few M), where the PN expansion is unlikely to be reliable. One can, however, construct PN waveforms in the EMRI limit, accepting their certain unreliability as a way to develop a very ''quick and dirty'' set of tools for studying these waves. PN EMRI waveforms are available for

systems of a test mass in a quasicircular [27] or eccentric [28] orbit around a Schwarzschild black hole, or in a quasicircular orbit around a slowly rotating Kerr black hole [29].

More recently, a class of approximate PN waveforms has been developed by Barack and Cutler [31]. These "analytic kludge" (AK) waveforms are essentially phenomenological waveforms—they are constructed using the classic quadrupole waveforms for eccentric Keplerian orbits derived in [54], but with the relativistic effects of pericenter precession, Lense-Thirring precession, and inspiral imposed. Though not as accurate as the NK waveforms described in this paper, the AK are very quick to generate, and have proven to be useful for computing the Fisher information matrix in investigations of parameter measurement with EMRI GWs [31].

The overlap between AK and NK waveforms is high in the very weak field, but degrades as the orbital periapse is decreased (see [20]; more detailed comparisons will be included in future papers on the semicoherent algorithm currently in preparation). Even for geodesic orbits, AK and NK waveforms with the *same physical parameters* drift out of phase quickly, since the frequency structure of the two waveform families is different. This arises because the AK uses a Keplerian orbital parametrization, compared to the geodesic parametrization used in the NK. For an equatorial orbit with semilatus rectum $p = 30M$ and eccentricity $e = 0.3$ around a $10^6 M_\odot$ black hole of spin $a = 0.8$, the azimuthal frequency of the NK waveform is 0.196 mHz compared to 0.216 mHz for the AK. These orbits will therefore be one cycle out of phase within ~6 hrs. AK waveforms will thus not be particularly *faithful* templates. The problems can be mitigated by adjusting the orbital parameters of the AK waveform to improve the match with the NK, and the AK waveforms do capture the main features of true EMRI waveforms. For this reason, they may be quite *effectual* templates, but this has not yet been properly assessed. In the future, the effectualness of the AK waveforms as detection templates will be investigated by using banks of AK templates to search for more accurate NK or TB waveforms embedded in noise.

C. Semirelativistic numerical kludge waveforms

The idea behind the numerical kludge (NK) waveforms is to combine an exact particle trajectory (up to inaccuracies in the phase space trajectory and conservative radiation-reaction terms) with an approximate expression for the GW emission. By including the particle dynamics accurately, we hope to capture the main features of the waveform accurately, even if we are using an approximation for the waveform construction.

The computation of NK waveforms proceeds in three steps. The first is to construct an inspiral trajectory in "phase space"—that is, the space of constants E (energy), L_z (axial angular momentum) and Q (Carter constant) which characterizes Kerr black hole orbits (up to initial conditions). The construction of the phase space trajectory has already been described in previous work [9,10]. In this paper we shall (in most cases) ignore the evolution of orbits due to radiation reactions. The procedure for waveform construction including orbital evolution is identical to that given here. The second step is to integrate the Kerr geodesic equations along the inspiral trajectory and hence obtain the Boyer-Lindquist coordinates of the inspiralling object as a function of time [33]. The final step is to construct a gravitational waveform from this inspiral trajectory. We do this by identifying the Boyer-Lindquist coordinates (r, θ, ϕ, t) with spherical polar coordinates in flat-space and then evaluating a flat-space emission formula for the corresponding flat-space source orbit.

The idea of coupling a weak-field formula with fully relativistic motion first appeared in papers by Sasaki and Ruffini [55,56] and was then investigated more thoroughly for a test-body orbiting a Schwarzschild black hole by Tanaka *et al.* [23]. More recently, Gair *et al.* [38] looked at semirelativistic fluxes for Schwarzschild orbits and derived analytic expressions for the fluxes from arbitrary orbits. Their focus was on highly eccentric orbits relevant to the capture problem. In all these cases, the authors were interested in computing semirelativistic fluxes, rather than waveforms. While our focus is on waveforms rather than fluxes, in Sec. IV C we do calculate semirelativistic fluxes for Kerr orbits, as these results have not yet appeared in the literature.

In the remainder of this section, we describe the two stages of waveform generation (ignoring backreaction): (i) the computation of a trajectory, and (ii) the computation of a gravitational waveform from an arbitrary trajectory.

1. Computing the orbital trajectory

The first step in constructing a numerical kludge waveform is to compute the trajectory that the inspiralling body follows in the Boyer-Lindquist coordinates of the Kerr spacetime of the central black hole. Ignoring radiation reaction, this path is a Kerr geodesic. Geodesic motion in the Kerr spacetime is well-known [57,58] and is governed by a set of first-order differential equations:

$$\Sigma \frac{dr}{d\tau} = \pm\sqrt{V_r}, \tag{1a}$$

$$\Sigma \frac{d\theta}{d\tau} = \pm\sqrt{V_\theta}, \tag{1b}$$

$$\Sigma \frac{d\phi}{d\tau} = V_\phi, \tag{1c}$$

$$\Sigma \frac{dt}{d\tau} = V_t, \tag{1d}$$

where the various "potentials" are defined by

$$V_r = [E(r^2 + a^2) - L_z a]^2 - \Delta[r^2 + (L_z - aE)^2 + Q], \tag{2a}$$

$$V_\theta = Q - \cos^2\theta\left[a^2(1 - E^2) + \frac{L_z^2}{\sin^2\theta}\right], \tag{2b}$$

$$V_\phi = \frac{L_z}{\sin^2\theta} - aE + \frac{a}{\Delta}[E(r^2 + a^2) - L_z a], \tag{2c}$$

$$V_t = a(L_z - aE\sin^2\theta) + \frac{r^2 + a^2}{\Delta}[E(r^2 + a^2) - L_z a]. \tag{2d}$$

Here, $\Sigma = r^2 + a^2\cos^2\theta$, and $\Delta = r^2 - 2Mr + a^2$. The constants E, L_z, Q are the three first integrals of the motion: E is the orbital energy; L_z is the projection of the orbital angular momentum along the black hole's spin axis; and Q is known as the "Carter constant". This last constant is the relativistic generalization of the "third integral" used to separate the equations which describe orbits in an axisymmetric gravitational potential (a result which is particularly well-known in the literature describing orbits in galactic potentials [59]). In the spherical (i.e., Schwarzschild) limit, Q reduces to the square of the orbital angular momentum projected into the equatorial plane; see [9] and references therein for discussion.

For a given E, L_z and Q, the roots of V_r determine the turning points of the radial motion—the periastron r_p, and apastron r_a. From these, one can define an orbital eccentricity e, and semilatus rectum p, using the conventional Keplerian definitions

$$r_p = \frac{p}{1 + e}, \qquad r_a = \frac{p}{1 - e}, \tag{3a}$$

$$\Rightarrow p = \frac{2r_a r_p}{r_a + r_p}, \qquad e = \frac{r_a - r_p}{r_a + r_p}. \tag{3b}$$

We also replace the Carter constant by an "inclination angle", defined by

$$\tan^2\iota = \frac{Q}{L_z^2}. \tag{4}$$

To aid numerical integration, one can work in terms of two angular variables, ψ and χ, instead of r and θ. We define ψ by the equation

$$r = \frac{p}{1 + e\cos\psi}. \tag{5}$$

We define χ by the equation $z = \cos^2\theta = z_-\cos^2\chi$, where z_- is given by

$$\beta(z_+ - z)(z - z_-) = \beta z^2 - z[Q + L_z^2 + a^2(1 - E^2)] + Q, \tag{6}$$

with $\beta = a^2(1 - E^2)$. Expanding the radial potential as

$$V_r = (1 - E^2)(r_a - r)(r - r_p)(r - r_3)(r - r_4), \tag{7}$$

we find evolution equations for ψ and χ of the form

$$\frac{d\psi}{dt} = \frac{M\sqrt{1 - E^2}[(p - r_3(1 - e)) - e(p + r_3(1 - e)\cos\psi)]^{1/2}[(p - r_4(1 + e)) + e(p - r_4(1 + e)\cos\psi)]^{1/2}}{[\gamma + a^2 E z(\chi)](1 - e^2)}, \tag{8}$$

$$\frac{d\chi}{dt} = \frac{\sqrt{\beta[z_+ - z(\chi)]}}{\gamma + a^2 E z(\chi)} \quad \text{where } \gamma = E\left[\frac{(r^2 + a^2)^2}{\Delta} - a^2\right] - \frac{2MraL_z}{\Delta}. \tag{9}$$

In terms of the variables ϕ, ψ and χ, the geodesic equations are well behaved at the turning points of the motion, which facilitates numerical integration (as discussed in [33]).

Although we mostly ignore it here, it is easy to include radiation reaction in this prescription. To do so, one first computes an inspiral trajectory through phase space by writing

$$\frac{dE}{dt} = f_E(a, M, m, p, e, \iota), \tag{10a}$$

$$\frac{dL_z}{dt} = f_L(a, M, m, p, e, \iota), \tag{10b}$$

$$\frac{dQ}{dt} = f_Q(a, M, m, p, e, \iota). \tag{10c}$$

The functions f_E, f_L and f_Q are derived from well-known post-Newtonian results, augmented by additional corrections. The leading order part of f_E is given in a later section of this paper, Eq. (46). (For the full expressions see Ref. [10]). Since the parameters a, M and m are constant, and p, e and ι are directly related to E, L_z and Q via Eqs. (3) and (4), Eqs. (10) can be integrated to give the phase space trajectory. That is, the values of E, L_z and Q (or equivalently p, e and ι) are given as functions of time. To obtain the trajectory of the inspiralling particle, these time dependent expressions can be substituted into the right hand sides of Eqs. (1c), (1d), (8), and (9). The resulting set of ODEs can then be integrated to give the inspiral trajectory. In the following (with one exception), we will only consider waveforms from geodesic trajectories (setting $f_E \equiv f_L \equiv f_Q \equiv 0$), and refer the reader to Refs. [9,10] for more details on the construction of inspirals.

Once a trajectory has been obtained in this manner, one constructs an "equivalent" flat-space trajectory by projecting the Boyer-Lindquist coordinates onto a fictitious

spherical polar coordinate grid, defining the corresponding Cartesian coordinate system and pretending that these new coordinates are true flat-space Cartesian coordinates:

$$x = r\sin\theta\cos\phi, \tag{11a}$$

$$y = r\sin\theta\sin\phi, \tag{11b}$$

$$z = r\cos\theta. \tag{11c}$$

We use the resulting flat-space trajectory as input to a wave generation formula. This is a "bead on a wire" prescription—by putting the trajectory in flat space, we remove the background that is causing the curvature of the geodesic path and hence we are forcing the particle to move along a curved path like a bead moving on a wire. This leads to obvious inconsistencies in the approach—e.g., the nonconservation of the flat-space energy-momentum tensor of the particle motion since we are not including the energy-momentum of "the wire" along which the particle moves.

2. Waveform generation

Having constructed the particle orbit in our pseudo-flat-space, we now apply a flat-space wave generation formula. Consider the weak-field situation and write down the spacetime metric as $g_{\mu\nu} = \eta_{\mu\nu} + h_{\mu\nu}$, where $\eta_{\mu\nu}$ is the flat metric and $h_{\mu\nu}$ are small perturbations. The *trace-reversed* metric perturbation is defined as $\bar{h}^{\mu\nu} \equiv h^{\mu\nu} - (1/2)\eta^{\mu\nu}h$, where $h = \eta^{\mu\nu}h_{\mu\nu}$. Imposing the Lorentz gauge condition $\bar{h}^{\mu\alpha}{}_{,\alpha} = 0$, the linearized Einstein field equations can be written as

$$\Box\bar{h}^{\mu\nu} = -16\pi\mathcal{T}^{\mu\nu}, \tag{12}$$

in which $\Box$ denotes the usual flat-space wave operator and the effective energy-momentum tensor $\mathcal{T}^{\mu\nu}$ satisfies

$$\mathcal{T}^{\mu\nu}{}_{,\nu} = 0. \tag{13}$$

Here a comma subscript denotes partial derivative ($f_{,\mu} = \partial f/\partial x^{\mu}$). Note that our source conservation equation uses a partial rather than a covariant derivative. This is because we would hope, in a self-consistent approach, to choose coordinates so that the energy-momentum tensor is flat-space conserved. Finally, when observing GWs at large distances, we are really only interested in the transverse and traceless parts of the spatial components of $\bar{h}^{jk}$; a projection of these components will be necessary.

Taking coordinates centered at the black hole, we denote the position of the observer by $(t, \mathbf{x})$ and the position of the particle by $(t_p, \mathbf{x}_p)$). The wave-equation (12) has the familiar retarded time solution

$$\bar{h}^{jk}(t, \mathbf{x}) = 4\int \frac{\mathcal{T}^{jk}(t - |\mathbf{x} - \mathbf{x}'|, \mathbf{x}')}{|\mathbf{x} - \mathbf{x}'|}\mathrm{d}^3x'. \tag{14}$$

The additional coordinate $\mathbf{x}'$ is the integration variable, which goes over every possible space location where the effective energy-momentum tensor $\mathcal{T}^{\mu\nu}(t', \mathbf{x}')$ is nonzero. If the source motion is only negligibly influenced by gravity, then $\mathcal{T}^{\mu\nu}$ may be taken to equal $T^{\mu\nu}$, the energy-momentum tensor of the matter source. In Ref. [36], Press derived a formula valid for extended, fast motion sources. This was obtained by substituting Eq. (13) into Eq. (14) repeatedly. The result is

$$\bar{h}^{jk}(t, \mathbf{x}) = \frac{2}{r}\frac{\mathrm{d}^2}{\mathrm{d}t^2}\int[(\mathcal{T}^{00} - 2\mathcal{T}^{0l}n_l + \mathcal{T}^{lm}n_ln_m)x'^jx'^k]_{t'=t-|\mathbf{x}-\mathbf{x}'|}\mathrm{d}^3x', \tag{15}$$

in which $r^2 = \mathbf{x}\cdot\mathbf{x}$ and $\mathbf{n} = \mathbf{x}/r$. In the slow motion limit, the Press formula reduces to the usual quadrupole formula (hereafter, an overdot denotes a time-derivative)

$$\bar{h}^{jk}(t, \mathbf{x}) = \frac{2}{r}[\ddot{I}^{jk}(t')]_{t'=t-r}, \tag{16}$$

where

$$I^{jk}(t') = \int x'^jx'^kT^{00}(t', \mathbf{x}')d^3x' \tag{17}$$

is the source's mass quadrupole moment. Including the next order terms (the mass octupole and current quadrupole moments of the source, denoted M^{ijk} and S^{ijk} respectively), we obtain the quadrupole-octupole formula (see Refs. [35,36] for details),

$$\bar{h}^{jk} = \frac{2}{r}[\ddot{I}^{jk} - 2n_i\ddot{S}^{ijk} + n_i\dddot{M}^{ijk}]_{t'=t-r}, \tag{18}$$

with

$$S^{ijk}(t') = \int x'^jx'^kT^{0i}(t', \mathbf{x}')d^3x', \tag{19}$$

$$M^{ijk}(t') = \int x'^ix'^jx'^kT^{00}(t', \mathbf{x}')d^3x'. \tag{20}$$

Note that in both Eqs. (16) and (18), the retarded time is $t - r$ instead of the more complicated expression appearing in (15). If desired, it is a straightforward (but increasingly tedious) task to include more terms in the slow-motion expansion of (15). In the present work we shall make use of Eqs. (16) and (18) and the full Press formula (15).

The waveform in the standard transverse-traceless (TT) gauge is given by the TT projection of the above expressions. We define an orthonormal spherical coordinate system via

$$\mathbf{e}_r = \frac{\partial}{\partial r}, \qquad \mathbf{e}_\Theta = \frac{1}{r}\frac{\partial}{\partial\Theta}, \qquad \mathbf{e}_\Phi = \frac{1}{r\sin\Theta}\frac{\partial}{\partial\Phi}. \tag{21}$$

The angles $\{\Theta, \Phi\}$ denote the observation point's latitude and azimuth, respectively. The waveform in transverse-

traceless gauge is then given by

$$h^{jk}_{\rm TT} = \frac{1}{2}\begin{pmatrix} 0 & 0 & 0 \\ 0 & h^{\Theta\Theta} - h^{\Phi\Phi} & 2h^{\Theta\Phi} \\ 0 & 2h^{\Theta\Phi} & h^{\Phi\Phi} - h^{\Theta\Theta} \end{pmatrix}, \tag{22}$$

with

$$h^{\Theta\Theta} = \cos^2\Theta[h^{xx}\cos^2\Phi + h^{xy}\sin 2\Phi + h^{yy}\sin^2\Phi] + h^{zz}\sin^2\Theta - \sin 2\Theta[h^{xz}\cos\Phi + h^{yz}\sin\Phi], \tag{23a}$$

$$h^{\Phi\Theta} = \cos\Theta\left[-\frac{1}{2}h^{xx}\sin 2\Phi + h^{xy}\cos 2\Phi + \frac{1}{2}h^{yy}\sin 2\Phi\right] + \sin\Theta[h^{xz}\sin\Phi - h^{yz}\cos\Phi], \tag{23b}$$

$$h^{\Phi\Phi} = h^{xx}\sin^2\Phi - h^{xy}\sin 2\Phi + h^{yy}\cos^2\Phi. \tag{23c}$$

The usual "plus" and "cross" waveform polarizations are given by $h^{\Theta\Theta} - h^{\Phi\Phi}$ and $2h^{\Theta\Phi}$ respectively. The expressions (15), (16), and (18) are valid for a general extended source in flat-space. If we specialize to the case of a point-mass μ moving along a trajectory $x'_p(\tau)$, we know that the energy-momentum tensor in flat spacetime is given by

$$T^{\mu\nu}(t', \mathbf{x}') = \mu \int_{-\infty}^{\infty} \frac{dx'^{\mu}_p}{d\tau}\frac{dx'^{\nu}_p}{d\tau}\delta^4(x' - x'_p(\tau))$$
$$d\tau = \mu \frac{d\tau}{dt'_p}\frac{dx'^{\mu}_p}{d\tau}\frac{dx'^{\nu}_p}{d\tau}\delta^3(\mathbf{x}' - \mathbf{x}'_p(t')), \tag{24}$$

where τ is the proper time along the trajectory. It is related to the particle's coordinate time by $d\tau = (1 - v^2/c^2)^{1/2}dt'$, where $v^2 = |d\mathbf{x}'_p/dt'_p|^2$. On the right hand side of Eq. (24) is a term $dt'_p/d\tau = 1 + O(v^2/c^2)$. Expressions (16) and (18) are slow-motion expansions and at the order of these expansions we should replace $dt'_p/d\tau$ by 1 for consistency. The Press formula (15) is a fast-motion expression, and therefore we do include this term. The presence of a δ-function in $T^{\mu\nu}$ facilitates the simplification of the various moments in Eqs. (16) and (18):

$$I^{jk} = \mu x'^{j}_p x'^{k}_p, \tag{25}$$

$$S^{ijk} = v^i I^{jk}, \tag{26}$$

$$M^{ijk} = x'^{i}_p I^{jk}. \tag{27}$$

Here $v^a \equiv dx'^a/dt'_p$. The Press formula similarly simplifies to

$$h^{jk}(t, \mathbf{x}) = \frac{2\mu}{r}\frac{d^2}{dt^2}\left[(1 - n_a v^a)x'^{j}_p x'^{k}_p\left(\frac{dt'_p}{d\tau}\right)\right]_{t'_p = t - |\mathbf{x} - \mathbf{x}'_p|}. \tag{28}$$

The square bracketed expression is to be evaluated at a time t'_p given implicitly by $t = t'_p + |\mathbf{x} - \mathbf{x}'_p(t'_p)|$. In a numerical implementation, we evaluate the expression as a function of the time t'_p along the particle's path. In order to obtain a time series that is evenly spaced in t and compute the right-hand side of Eq. (28) by finite-differencing, we adjust the spacing of the sampling at the particle, $\delta t'_p$, such that

$$\delta t = (1 - n_a v^a)\delta t'_p. \tag{29}$$

With a delta function source (24), the retarded-time solution (14) can be evaluated directly [55]:

$$\bar{h}^{jk}(t, \mathbf{x}) = \left[\frac{4\mu}{r}\left(\frac{dt'_p}{d\tau}\right)\frac{dx'^{j}_p}{dt'_p}\frac{dx'^{k}_p}{dt'_p}\frac{1}{1 - n_a v^a}\right]_{t'_p = t - |\mathbf{x} - \mathbf{x}'_p|}. \tag{30}$$

Naively, one could suppose that (30) will perform better than (15), since it is derived using only one of the two (invalid) flat space equations, rather than both. In fact, we find that the retarded integral expression (30) performs much worse than either (16), (18) or (15) when compared to TB waveforms. The reason appears to be that the manipulations which lead to the quadrupole, quadrupole-octupole, and Press formulae ensure that the actual source terms—mass motions—are on the right hand side. This is to be contrasted with the retarded integral expression (14), which identifies the dominant GW on the left hand side with weak spatial stresses on the right.

We must emphasize that the NK prescription is clearly inconsistent—we are binding the particle motion to a Kerr geodesic while assuming flat spacetime for GW generation and propagation. This is manifested by the fact that the energy-momentum tensor (24) is not flat-space conserved, $\partial_\nu T^{\mu\nu} \neq 0$. However, the spirit of this calculation is *not* a formal and consistent approximation to EMRI waveforms; it is rather a "phenomenological" approach which takes into account those pieces of physics we believe are the most crucial—in particular, the exact Kerr geodesic motion. By including the exact source trajectory, we ensure that the spectral components of the kludge waveforms are at the correct frequencies, although their relative amplitudes will be inaccurate. As we shall see, this line of

thinking is validated *post facto* by the remarkable agreement between the kludge and TB waveforms (see Sec. IV).

It is important to underline the physical assumptions that have been made in the derivation of (15), (16), and (18), in order to understand their generic limitations. First of all, the assumed absence of any background gravitational field means that our kludge waveforms are unable to capture any features related to backscattering. This effect is known to first appear at 1.5PN [i.e. $\mathcal{O}(v^3)$] level (see, e.g., [60]). Such "tails" of waves are particularly prominent in the strong-field TB equatorial "zoom-whirl" waveforms [15] and in the waveforms from plunging or parabolic orbits [61]. In all these cases, the hole's quasinormal mode ringing adorns the emitted signal.

The slow-motion nature of expressions (16) and (18) suggests that they might be bad models for waveforms generated by orbits venturing deep inside the central BH's spacetime. The rich multipole structure of the true waveform from such orbits is poorly reproduced, as any slow-motion approximation essentially truncates the sum over multipoles. The Press formula (15) includes contributions at all multipoles and so might be expected to handle these contributions quite well. However, it turns out that it does not perform that much better than the quadrupole-octupole waveform in this regime. While it includes contributions at all multipoles, the lack of background curvature in the waveform model means that the amplitude of the higher modes is much lower than expected for true EMRI waveforms.

Fortunately, these two deficiencies become important for the same class of orbits—those that allow the body to approach very close to the black hole. As a rule of the thumb we shall find that NK waveforms are reliable (in terms of the overlap discussed in the next section) as long as the closest orbital approach (periastron) is $r_p \gtrsim 5M$.

III. THE OVERLAP BETWEEN WAVEFORMS

We now give a brief description of the measure used for the quantitative comparison between NK and TB waveforms. The main motivation for the computation of accurate EMRI waveforms is to carry out matched filtering for detection of the GWs. For the purpose of signal detection and parameter estimation, a bank of templates is constructed which covers the desired parameter space with sufficient resolution. The detector output is then filtered through each template. The measured strain amplitude in the detector, $x(t) = s(t) + n(t)$, consists of a (possibly present) signal $s(t)$, and the detector noise $n(t)$. We define the Fourier representation of these time series as

$$\tilde{x}(f) = \int_{-\infty}^{\infty} x(t) e^{-i2\pi tf} dt. \tag{31}$$

The signal-to-noise ratio (SNR) can be expressed in terms of an inner product defined on the vector space of possible signals. Given two vectors (time series), $x(t_k)$, $h(t_k)$, we define the overlap $(x|h)$ by the equation [62,63]

$$(x|h) = 2 \int_0^{+\infty} \frac{\tilde{x}(f)\tilde{h}^*(f) + \tilde{x}^*(f)\tilde{h}(f)}{S_h(f)} df, \tag{32}$$

where $S_h(f)$ is the one-sided noise power spectral density (PSD) (in this case, the noise PSD for the LISA detector) and an asterisk denotes complex conjugation. Considering $h(t_k, \lambda^\alpha)$ as a template with parameters λ^α we can approximate the SNR by [62]

$$\frac{S}{N}[h(\lambda^\alpha)] = \frac{\langle (s|h) \rangle_n}{\sqrt{\langle (n|h)^2 \rangle_n}} = \frac{(s|h)}{\sqrt{(h|h)}}. \tag{33}$$

The notation $\langle f \rangle_n$ means to ensemble average the function f over all possible noise realizations n. The PSD in the denominator of Eq. (32) serves to suppress those frequency components of the signal at which the detector noise is large.

The main tool which will be used in this paper is not the SNR, but rather the overlap function $\mathcal{O}$. The overlap is defined as an inner product between two normalized vectors/signals:

$$\mathcal{O} = (\hat{s}|\hat{h}). \tag{34}$$

The normalization is chosen so that $(\hat{s}|\hat{s}) = (\hat{h}|\hat{h}) = 1$. The overlap can be regarded as the inner product between two unit vectors; it varies within $[-1, 1]$. The overlap is equal to 1 if the two waveforms are identical, and it equals zero if the two waveforms are orthogonal (for example, cosine and sine signals). The overlap is an appropriate measure of "goodness-of-fit" since we are interested in knowing how well the NK approximate the behavior of TB EMRI waveforms. In this context, it is important to include the noise properties of the detector since it is no problem if a template has poor performance at frequencies where detector noise is large.

For a fair comparison, we should choose the signal (TB waveform) and template to have the same parameters.[2] In practice, the start times of our signals and templates were slightly mismatched, so we allow for maximization over starting time ("time of arrival"). This maximization is commonly done in GW data analysis, and can be accomplished very efficiently in the Fourier transform, since the time offset corresponds to a phase shift in the frequency

[2]Note that here we study not the fitting factors but the faithfulness of the NK waveforms as compared to TB-based ones, i.e., how well an approximate waveform with given parameters reproduces the "true" waveform with the *same* physical parameters. A faithful bank of waveforms could be used for parameter estimation, while for detection all that is required is an "effectual" template bank, i.e., one in which every true waveform is well represented by one template, even if that template has very different parameters [64].

domain. Accordingly, we modify the inner product $(x|h)$ slightly:

$$(x|h) = \max_t\left(\int \frac{\tilde{x}(f)\tilde{h}^*(f) + \tilde{x}^*(f)\tilde{h}(f)}{S_h(f)} e^{i2\pi f t} df\right) \quad (35)$$

where t corresponds to the time difference. We find that the maximum usually occurs with an time offset close to zero (typically a few bins).

We conclude our discussion of the overlap by describing our approximation to the LISA noise $S_h(f)$. We have used an analytic approximation to the numerically generated sensitivity curve given in Ref. [65]. The agreement between these two curves is excellent as clearly illustrated in Fig. 1. Our approximate $S_h(f)$ function can be easily calculated according to the following simple prescription. Define $u = 2\pi f\tau$, where f is frequency and $\tau = (5 \times 10^6 \text{ km})/c = 50/3$ sec is the light travel time down one of LISA's arms. For $u < u_{\text{trans}} = 0.25$ we set

$$S_h(f) = \frac{8.08 \times 10^{-48}}{(2\pi f)^4} + 5.52 \times 10^{-41}, \quad (36)$$

while for $u \geq u_{\text{trans}}$,

$$S_h(f) = \frac{1}{R}\left(\frac{2.88 \times 10^{-48}}{(2\pi f)^4} + 5.52 \times 10^{-41}\right), \quad (37)$$

where

$$R = \frac{1}{u^2}\left[(1 + \cos^2(u))\left(\frac{1}{3} - \frac{2}{u^2}\right) + \sin^2(u) + \frac{4\sin(u)\cos(u)}{u^3}\right]. \quad (38)$$

Note that LISA's characteristics are incorporated in the light travel time τ and in the numerical constants in the above expressions, so a similar mission but with different noise characteristics would still be described by the functional form defined by Eqs. (36)–(38).

We have also included noise from a confused population of galactic white dwarf binaries following the prescription outlined in [31].

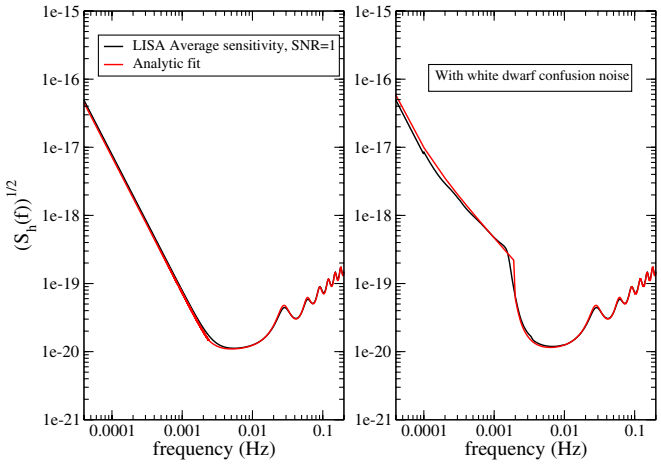

FIG. 1 (color online). Expected sensitivity curve $\sqrt{S_h(f)}$ for LISA; black curve: numerical curve as generated in [65], red curve: analytic approximation used in this paper, see text for details).

IV. KLUDGE WAVEFORMS AND FLUXES: RESULTS

A. Comparison to Teukolsky-based geodesic waveforms

1. Time-domain comparison

In this Section we compare NK waveforms (using the overlap function defined in the previous Section) to a variety of TB waveforms from inclined-circular, equatorial-eccentric and some generic Kerr orbits. The TB waveforms are treated here as "exact" (though this is not strictly the case as discussed in Sec. II). Our comparison rule is that the waveforms are generated using the same Kerr orbit with identical initial conditions. We label these orbits by the triad of orbital elements $\{p, e, \iota\}$ defined in Eqs. (3) and (4).

Figs. 2–4 show time-domain waveforms for a selection of orbits in the moderate and strong field. The NK waveforms plotted in these figures were generated by using the quadrupole-octupole formula (18). The results for plus and cross polarizations are essentially the same, so in the figures we show only the plus polarization. For all of the

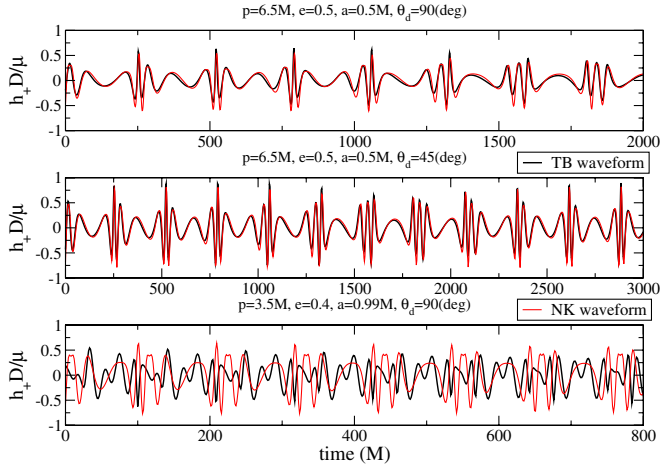

FIG. 2 (color online). Comparing TB and quadrupole-octupole kludge waveforms (black and red curves (bold black and gray curves in the b&w version), respectively) for equatorial orbits and for an observer at a latitudinal position $\theta = 45°$ or $90°$. Orbital parameters are listed above each graph. The waveforms are scaled in units of D/μ where D is the radial distance of the observation point from the source and μ is the test-body's mass. The x axis measures retarded time (in units of M) and we are showing the '+' polarization of the GW in each case. The overlaps between the NK and TB waveforms are 0.970, 0.987, 0.524 going from the top figure down.

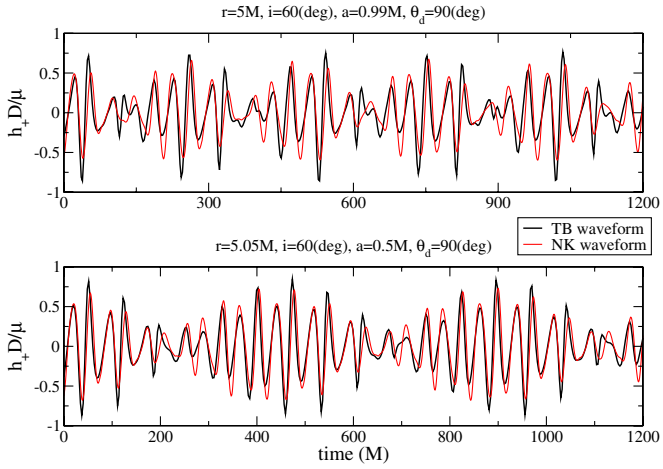

FIG. 3 (color online). Comparing TB and quadrupole-octupole kludge waveforms (black and red curves (bold black and gray curves in the b&w version), respectively) for circular-inclined orbits and for an observer at a latitudinal position $\theta = 90°$. Orbital parameters are listed above each graph. The waveforms are scaled in units of D/μ where D is the radial distance of the observation point from the source and μ is the test-body's mass. The x axis measures retarded time (in units of M) and we again show the plus polarization of the GW. The overlaps between the NK and TB waveforms are 0.882 for the top figure and 0.955 for the bottom figure.

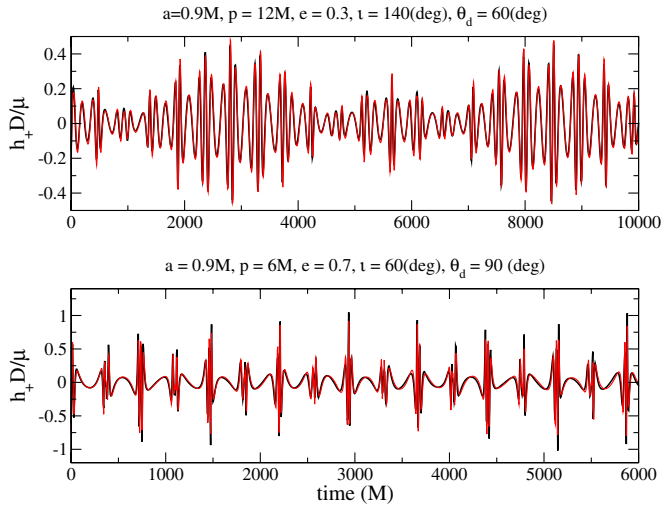

FIG. 4 (color online). Comparing TB and quadrupole-octupole kludge waveforms (black and red curves (bold black and gray curves in the b&w version), respectively) for generic orbits. Orbital parameters are listed above each graph. The waveforms are scaled in units of D/μ where D is the radial distance of the observation point from the source and μ is the test-body's mass. The x axis measures retarded time (in units of M). The overlaps between the NK and TB waveforms are 0.991 and 0.966 for the top and bottom figures, respectively.

figures, we have assumed an observation point located at $\Phi = 0°$ and $\Theta = 45°$ or $90°$ (as indicated).

Direct visual inspection of the waveforms gives some indication of how well the NK and TB waveforms match. In each of the cases illustrated, the kludge waveforms manage to capture the overall wave pattern, and for the orbits with $p > 8M$ they almost exactly match the TB waveforms. For ultrarelativistic orbits (e.g., with $p \lesssim 5M$ and $1 - a/M \ll 1$), the finer structure in the TB waveforms is clearly not reproduced by the quadrupole-octupole kludge waveforms. As we have discussed, these features are the imprints of higher multipole components in the radiation which are amplified by backscattering, and thus are not expected to appear in the NK waveforms. Waveforms generated using the Press formula (not shown) do have some finer features due to the presence of higher multipole components, as we might have hoped, but they are not nearly as complicated as the structure of the TB waveforms.

One also notices that for certain parts of the waveforms (e.g., Fig. 3), there is a disagreement in the amplitude while the phase is accurately reproduced. This amplitude discrepancy is periodic, i.e., the points where the amplitude is poorly reproduced occur at regular intervals. This suggests that the kludge waveforms are missing some periodic components, as we might expect since they are truncated expansions in multipole moments. Indeed, the amplitude discrepancy is less pronounced in the Press waveform, which includes contributions at all multipoles. For the purposes of data analysis, it is important to have templates with a high overlap with the true signals, and to achieve that it is much more important that the waveform phase is reproduced rather than the waveform amplitude. The waveform phase is determined by the orbit generating the gravitational radiation. The fact that the kludge waveforms are based on true geodesic orbits is presumably the reason that we find, *post facto*, such impressively high overlaps with TB waveforms and especially for those from circular-inclined orbits.

A comprehensive set of data for the overlaps between NK and TB waveforms is given in Tables I, II, and III in the Appendix. These were computed using the overlap function described in Section III and assuming a central black hole mass of $M = 10^6 M_\odot$. This was chosen since preliminary event rate estimates suggest the inspirals of $\sim 10 M_\odot$ BHs into $\sim 10^6 M_\odot$ SMBHs will dominate the LISA detection rate [20]. These tables indicate that if the orbital periastron $r_p \gtrsim 5M$, the overlap between TB waveforms and both the quadrupole-octupole and Press waveforms stays above ~ 0.95. We also find that both these expressions have better performance than the pure quadrupole waveforms (16), but there is little difference between quadrupole-octupole and Press waveforms. The kludge and TB waveforms begin to deviate significantly for strong-field, ultrarelativistic orbits with $r_p \lesssim 4M$, with the overlap dropping to $\sim 50\%$ for orbits that come very close to the horizon. Disappointingly, the Press waveforms do not seem to do much better than the quadrupole-

octupole waveforms in this strong-field regime, despite the inclusion of additional multipole components. The Press waveforms include only the "direct" contribution to the higher multipoles, i.e., the piece that arises from fast motion in flat spacetime. In true EMRI GWs, the higher multipole contributions are significantly enhanced by "tail" effects, i.e., the backscattering of radiation from the background geometry. Since we are using the Press formula in flat space, we do not include this backscattering enhancement. This is presumably why using the kludge Press waveforms does not significantly improve the overlap with TB waveforms. The Press waveforms do perform consistently better for circular orbits and weak-field eccentric orbits, but the difference between the two approaches is usually small (with the exception of a few cases which we discuss in more detail later). We conclude that the quadrupole-octupole waveform model is sufficient and there is not much gain from using the computationally more intensive Press formula.

To summarize, we find that kludge waveforms are accurate—and very quick to generate—substitutes for TB waveforms for all orbits with periapse $r_p \gtrsim 5M$. In Schwarzschild, the separatrix between bound and plunging orbits is at $(r_p)_S = (6 + 2e)/(1 + e)M$, so the kludge waveforms will be accurate throughout any inspiral with eccentricity at plunge $e \lesssim 1/3$. Computations of inspirals into Schwarzschild black holes [10] indicate that, in many cases, the residual eccentricity at plunge will be small, so that kludge waveforms will be suitable for the majority of Schwarzschild inspirals. For retrograde orbits around Kerr black holes ($90° \leq \iota \leq 180°$), the minimal periapse is at even larger radii, so that even weaker restrictions must be imposed on the eccentricity at plunge for the kludge to be valid. In contrast, for prograde orbits ($0° \leq \iota \leq 90°$), an increased black hole spin allows stable orbits to exist much deeper in the strong field. For $a = 0.9M$, the separatrix for circular orbits is at $r_p \approx 2.3M, 2.6M, 3.7M$ for orbits with inclinations of 0°, 30°, 60° respectively; for orbits with a plunge eccentricity of $e = 1/3$, it is at $r_p \approx 2.0M$, $2.2M$, $3.1M$ for the same inclinations. As $a \rightarrow M$, the separatrix of equatorial orbits decreases even more, asymptotically approaching $(r_p)_K^{\rm pro} = M$ [15]. Kludge waveforms are not particularly good in this regime, with overlaps ~50%; fortunately, this corresponds to a comparatively small region of parameter space. The evolution proceeds through this region very quickly, so we do not lose much signal-to-noise ratio by failing to match the waveforms in this region.

If the overlap between a given signal and the best-fit template in a search bank is less than 1, this leads to a decrease in the maximum distance to which that signal can be detected, and a corresponding reduction in event rate. For the purposes of detection, overlaps as low as 50% might well be considered good enough, if the astrophysical event rate is sufficiently large [20]. However, for the purposes of parameter estimation, much higher overlaps ($\gtrsim 95\%$) will be required in general. It is clear from the results in this paper that this is only partially achievable by the existing family of kludge waveforms. Nonetheless, these waveforms might be useful for LISA data analysis as search or detection templates over some (perhaps a large part) of the astrophysically relevant portion of the $\{a/M, p, e, \iota\}$ parameter space. The waveforms may also provide sufficiently accurate estimation of the source parameters (in certain regions of parameter space) that they could be used as the first stage in a hierarchical search. The purpose of such a search would be to identify "interesting" regions of parameter space for follow up with more accurate waveforms. This is the main conclusion of this paper.

However, the regions where kludge waveforms are good enough must be identified more carefully by comparison to accurate *inspiral* waveforms. As we have discussed earlier, the flat-space emission formula used in the construction of the NK waveforms ignores all effects of scattering from the background curvature. These tail terms make a significant contribution to the waveform structure, and build up over the course of an inspiral. Although we have found good overlaps with geodesic waveforms and circular-inclined inspiral waveforms (see Sec. IV B), comparisons to inspirals of eccentric-inclined orbits are required to properly assess the importance of including the tail terms. Accurate, self-force waveforms for such orbits will not be available for a few years and only then will it be possible to firmly demarcate the regime of usefulness of the present, or further improved, NK waveforms.

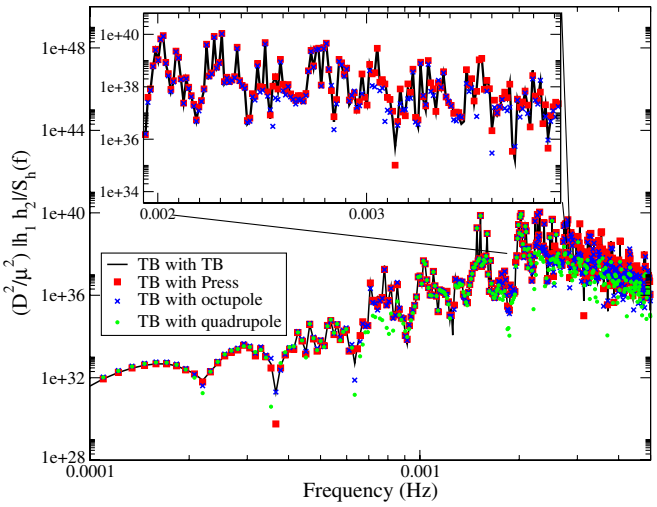

FIG. 5 (color online). Comparison of the integrand of the SNR in the frequency domain $[\tilde{h}(f)\tilde{s}^*(f)]/S_h(f)$ where $\tilde{h}(f)$ is determined from the quadrupole, quadrupole-octupole and Press waveforms, and $s(f)$ is determined from the TB waveform. We have chosen orbital parameters $p = 12M$, $e = 0.1$, $\iota = 120°$ and spin $a = 0.9M$. One can see that Press waveform performs better than quadrupole-octupole waveform at high frequencies.

2. Frequency domain comparison

To better understand the overlaps quoted in the tables we consider here the integrand of Eq. (35) for the value of t which maximizes the overlap:

$$\frac{\tilde{x}(f)\tilde{h}^*(f) + \tilde{x}^*(f)\tilde{h}(f)}{S_h(f)} e^{i2\pi f t}. \tag{39}$$

In Fig. 5 we plot this function for the generic orbit $p = 12M$, $e = 0.1$, $\iota = 120°$ and $a = 0.9M$. For the signal $\tilde{x}(f)$ we use the TB waveform and correlate it with templates $\tilde{h}(f)$. As templates we use the TB waveform itself (black solid line), the Press waveform (squares), the quadrupole-octupole NK waveform (crosses) and the quadrupole NK waveform (circles). We have deliberately chosen a case for which including higher harmonics significantly ($> 10\%$) improves the overlap, especially in the presence of white dwarf confusion noise (see Table III).

One can see that the main contributions to the overlap come from several dominant harmonics. For a circular equatorial orbit the main harmonic would correspond to twice the orbital frequency, but in general the main harmonics depend on eccentricity [31]. Besides the harmonics coming from the azimuthal motion there are many additional components coming from beating between harmonics of the fundamental frequencies of the ϕ-, θ- and r-motion: Ω_ϕ, Ω_θ, Ω_r (see [66] for a Fourier decomposition of the orbital motion). Depending on the mass M of the central BH, the dominant harmonics may lie in the most sensitive part of LISA's frequency range or they can be suppressed by confusion noise. In the latter case the higher harmonics, although smaller in amplitude, are effectively enhanced by the inverse power spectral density and therefore play an important role in SNR accumulation. Looking at the inlaid box in Fig. 5 we can compare the quadrupole-octupole and Press waveforms at high frequency. Here, the Press waveform does perform better—e.g., around 3 mHz the quadrupole-octupole NK waveform has failed to reproduce some harmonics in the TB signal, whereas the Press waveform does so pretty well. We will discuss the frequency representation of the signals further in the next subsection.

B. Comparison to Teukolsky-based inspiral waveforms

As described earlier, most of the existing TB waveforms describe GW emission from geodesic orbits, which is why we have focused on these for the comparisons above. However, TB waveforms have also been constructed for the inspiral of circular-inclined orbits [37]. To illustrate the applicability of the kludge to the detection of realistic, inspiralling EMRI waveforms, we here compare a kludge inspiral waveform to a TB circular-inclined inspiral waveform generated using the method described in [37]. The kludge inspiral trajectory is constructed using the flux

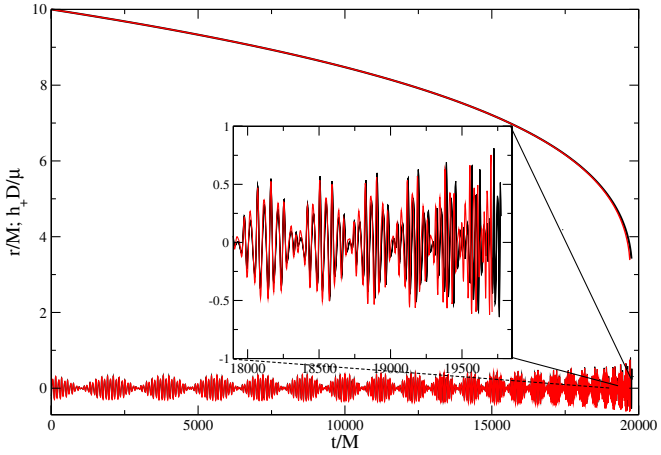

FIG. 6 (color online). The orbital evolution, $r(t)$, and h_+ polarization of the GW signal, for an inspiralling quasicircular-inclined orbit with initial parameters $p = 10M$, $e = 0$, $\iota = 45°$ and $a = 0.9M$, $\mu/M = 10^{-2}$, $\Theta = 90°$. The black curve corresponds to the TB waveform and the red (gray in b&w version) line represents the quadrupole-octupole NK waveform. The inlaid box shows the part of the waveform where the TB and NK results start to deviate, which correlates with the deviation in the inspiral.

formulae described in [10], and then the particle trajectory is computed as discussed in Sec. II C 1. We use the quadrupole-octupole formula (18) to generate a kludge waveform from this trajectory.

A visual comparison is shown in Fig. 6. There we plot both the inspiral trajectory $r(t)$ and the gravitational waveform h_+. One can see an excellent agreement up to the last several cycles, where we would not trust either type of waveform anyway. We have used a large mass ratio (10^{-2}) to compute the waveforms in order to speed up the orbital evolution. We should point out that the comparison is not improved if we use Press waveforms instead of quadrupole-octupole waveforms.

We may quantify the agreement in the waveforms by again using the overlap function, which we plot as a function of truncation time in Fig. 7 for three different masses of the central black hole. One can see that for the majority of the inspiral we obtain quite high overlap, but it decreases when we include the final stages of the inspiral. For the inspiral in Fig. 6, the overlap (when $M = 10^6 M_\odot$ and in presence of the white dwarf background) up until radii of $r = 8M$, $6M$, $5M$, $4M$, $3.5M$ is 0.985, 0.974, 0.92, 0.79, 0.755, respectively. The overlap over the whole inspiral is still greater than 75%. An overlap of 75% corresponds to a factor of $\sim$2 reduction in event rate. However, overlaps of 90% or 95% correspond to a reduction in event rate of only 1.4 or 1.17, respectively. A significant amount of signal-to-noise ratio accumulates over the early stage of inspiral, and so it may well be that kludge inspiral waveforms can be used to efficiently detect and track events until they reach $r \approx 5$–$6M$. Alternative techniques could

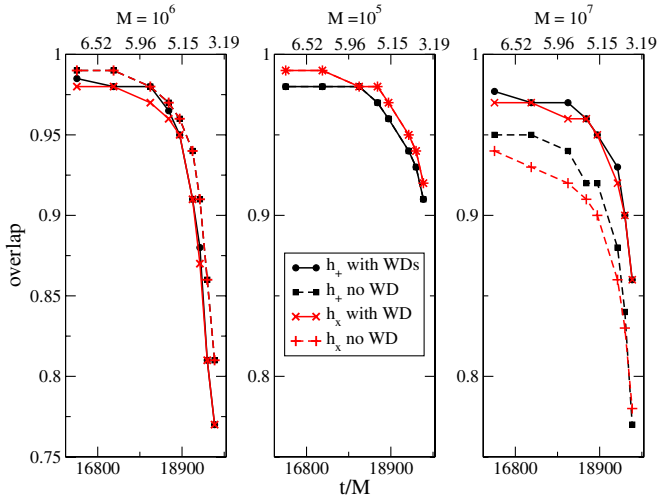

FIG. 7 (color online). Overlap between TB and NK waveforms (h_+ and $h_\times$) for an inspiralling (quasi)circular-inclined orbit as a function of truncation time. We show overlaps for different masses of the central BH: $M = 10^5, 10^6, 10^7 M_\odot$ and for sensitivity curves with and without white dwarf (WD) confusion noise. One can see that the overlap drops as we increase the truncation time and the mass M. On the top horizontal axis we show the orbital radius r/M corresponding to the truncation time. For $M = 10^5 M_\odot$ the lines with and without WD confusion lie on top of each other.

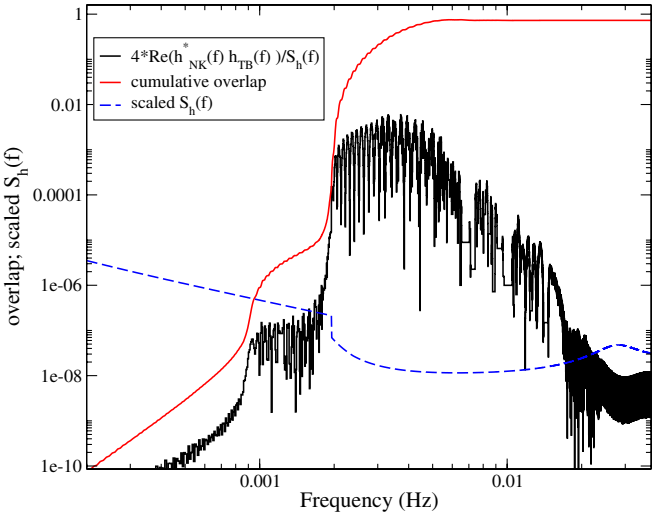

FIG. 8 (color online). The integrand of the overlap between TB and NK waveforms in the frequency domain (solid black line). Breaks in the curve correspond to a negative correlation. We also overplot the accumulative overlap (red solid line) and scaled $S_h(f)$ as a dashed blue line.

then be employed for detection during the latter stages of inspiral.

The mass of the central BH determines the frequency range through which the inspiral occurs. One could also evaluate the spectrum of the signal as a function of the dimensionless frequency (Mf)—the effect of changing M is then to shift the PSD $S_h(f)$ right as M is increased or shift it left as M is decreased. In Fig. 9 we again plot the overlap integrand (39) for $M = 10^6 M_\odot$. We also overplot the cumulative overlap

$$2\int_0^F \frac{\tilde{x}(f)\tilde{h}^*(f) + \tilde{x}^*(f)\tilde{h}(f)}{S_h(f)} df$$

and a scaled PSD. By shifting $S_h(f)$ on the plot left/right one can see how the central mass affects the amount each harmonic contributes to the SNR/overlap. The higher harmonics are modeled less accurately by NK waveforms and this leads to an overall drop in the overlap for $M = 10^7 M_\odot$. However, the majority of the high frequency contribution to the waveforms comes from the end of the inspiral which we do not reproduce very accurately, rather than from higher harmonics emitted during the earlier, moderately relativistic part of the orbit.

We should also mention that there is a problem with spectral leakage [67] (due to the large dynamic range) in the estimation of GW spectra. This is not a big problem on its own but for high M this leakage (at high frequencies) is amplified by the inverse power spectral density and leads to an erroneous result. In order to reduce this effect we have applied a window function

$$w(t) = \tfrac{1}{2}(1 + \tanh[A(t - \kappa T)] + \tanh[A(T - t - \kappa T)])$$

to the template and signal for $M = 10^7 M_\odot$ and in the presence of confusion noise. The parameters κ and A govern the steepness and cut-off point of the window; T is the waveform's duration. This function reduces the effect of the end of inspiral on the overlap and leads to an artificial increase in the overlap by a few percent.

As mentioned above, a significant amount of signal-to-noise ratio accumulates over the early stages of the inspiral. To illustrate this we show in Fig. 8 the accumulation of SNR as a function of time. To generate this plot, we have assumed the TB waveform is the signal and have used the NK waveform, truncated at different times, as the search template. One can see that we can recover up to 85% of the maximum SNR (i.e., the SNR if the template and signal were identical). Including the last few waveform cycles we see a drop in the SNR ($\sim 8\%$) due to the mismatch in the waveforms at the end of the inspiral.

Employing Press waveforms helps to improve overlaps further, but for ultrarelativistic orbits the omitted tail contribution to the waveform becomes increasingly significant.

C. Comparison to Teukolsky-based and PN fluxes

It is possible to construct expressions for the flux of energy and angular momentum carried by the kludge GWs, and use these as estimates of the energy and angular

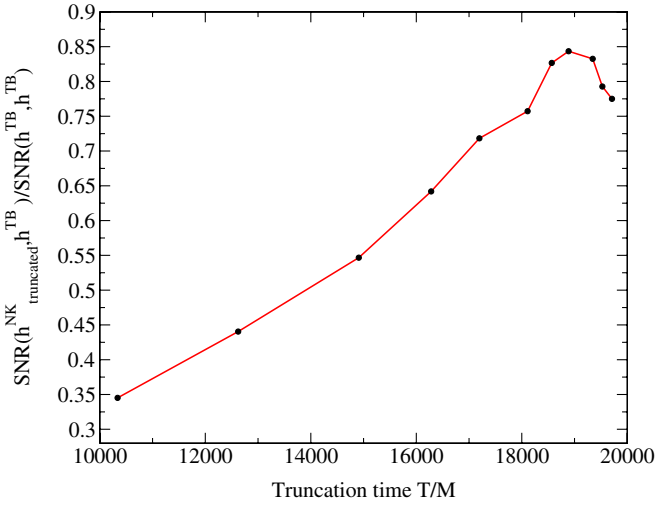

FIG. 9 (color online). In this plot we present SNR obtained by applying the truncated NK waveform as a template to the full inspiral represented by TB waveform: $\mathrm{SNR}(h^{\mathrm{NK}}_{\mathrm{tr}}, s^{\mathrm{TB}}) = \frac{(h^{\mathrm{NK}}_{\mathrm{tr}}|s^{\mathrm{TB}})}{(h^{\mathrm{NK}}_{\mathrm{tr}}|h^{\mathrm{NK}}_{\mathrm{tr}})^{1/2}}$ normalized by the total SNR: $\mathrm{SNR}(s^{\mathrm{TB}}, s^{\mathrm{TB}}) = (s^{\mathrm{TB}}|s^{\mathrm{TB}})^{1/2}$. The primary mass was taken to be $10^6 M_\odot$ and the sensitivity curved contained WD confusion noise. The total SNR for the source at 10 Gpc is approximately 66 (high SNR is due to large (10^{-2}) mass ratio).

momentum lost from the orbit in a true inspiral. The energy and angular momentum content of a TT GW field, h^{jk}_{TT}, propagating in flat space at large distances from the source is determined from the Isaacson energy-momentum tensor of the wave field [68,69]

$$T^{\mu\nu}_{\mathrm{GW}} = \frac{1}{32\pi}\langle h^{jk,\mu}_{\mathrm{TT}} h^{jk,\nu}_{\mathrm{TT}}\rangle. \tag{40}$$

Integration of this expression gives the energy and angular momentum loss rates due to GW emission (equations (4.13) and (4.22′) of [70]) as

$$\dot{E} = \frac{1}{16\pi}\int \langle h^{jk,t}_{\mathrm{TT}} h^{jk,t}_{\mathrm{TT}}\rangle r^2 \mathrm{d}\Omega \tag{41}$$

$$\dot{L}_i = \frac{1}{16\pi}\int \left\langle \epsilon_{ipq} h^{pa}_{\mathrm{TT}} h^{aq,t}_{\mathrm{TT}} - \frac{1}{2}\epsilon_{ipq} x_p h^{ab,q}_{\mathrm{TT}} h^{ab,t}_{\mathrm{TT}} \right\rangle r^2 \mathrm{d}\Omega. \tag{42}$$

Using the quadrupole-octupole formula to generate h^{jk}_{TT}, these expressions may be written in terms of the multipole moments of the source as

$$\langle \dot{E}\rangle = -\frac{1}{5}\left\langle I^{jk(3)}_{\mathrm{TT}} I^{jk(3)}_{\mathrm{TT}} + \frac{5}{189} M^{jkl(4)}_{\mathrm{TT}} M^{jkl(4)}_{\mathrm{TT}} + \frac{16}{9} J^{jk(3)}_{\mathrm{TT}} J^{jk(3)}_{\mathrm{TT}} \right\rangle \tag{43}$$

$$\langle \dot{L}_i\rangle = -\frac{2}{5}\epsilon^{ikl}\left\langle I^{ka(2)}_{\mathrm{TT}} I^{al(3)}_{\mathrm{TT}} + \frac{5}{126} M^{kab(3)}_{\mathrm{TT}} M^{lab(4)}_{\mathrm{TT}} + \frac{16}{9} J^{ka(2)}_{\mathrm{TT}} J^{qa(3)}_{\mathrm{TT}} \right\rangle. \tag{44}$$

In these expressions $J^{ij}_{\mathrm{TT}} = \epsilon_{jlm} S^{mli}_{\mathrm{TT}}$ and bracketed numbers in superscripts denote the number of time derivatives, e.g., $I^{ka(2)}_{\mathrm{TT}} = \mathrm{d}^2(I^{ka}_{\mathrm{TT}})/\mathrm{d}t^2$. If the kludge waveform is computed using the quadrupole formula (16), only the leading order I^{jk}_{TT} terms remain. If a Press waveform is used, there is an infinite sum of multipole components, and therefore expressions (41) and (42) must be employed directly.

The angle brackets in expressions (41)–(44) mean "average over several gravitational wavelengths". This is achieved by taking a time average of the instantaneous flux expression inside the angle brackets, i.e.,

$$\langle X\rangle = \frac{1}{T}\int_0^T X dt, \tag{45}$$

where T is an appropriate averaging time. It is important to ensure that this averaging time is long enough. For circular equatorial orbits, the symmetries of the system ensure that the instantaneous and averaged fluxes are identical. For an eccentric-equatorial orbit, there is only one periodicity in the flux—the period of the radial motion. Thus integrating over one radial period is sufficient to give an accurate average flux. For generic orbits, the averaging is more complicated since the periods of the motion in the radial and θ directions are in general different and noncommensurate. The averaging time therefore has to be long enough to encompass several periods of both motions. We illustrate this in Fig. 10 by plotting $\dot{E}$ as function of T for a generic orbit with parameters $p = 4M$, $a = 0.99M$, $\iota = 60°$ and

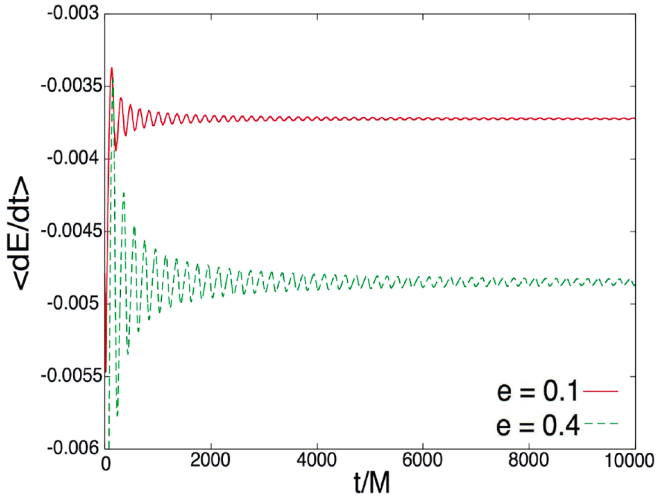

FIG. 10 (color online). Convergence of the averaged energy flux $\langle \dot{E}\rangle$ with respect to the averaging time T for a pair of equatorial-eccentric orbits. Note the increased convergence rate with decreasing eccentricity.

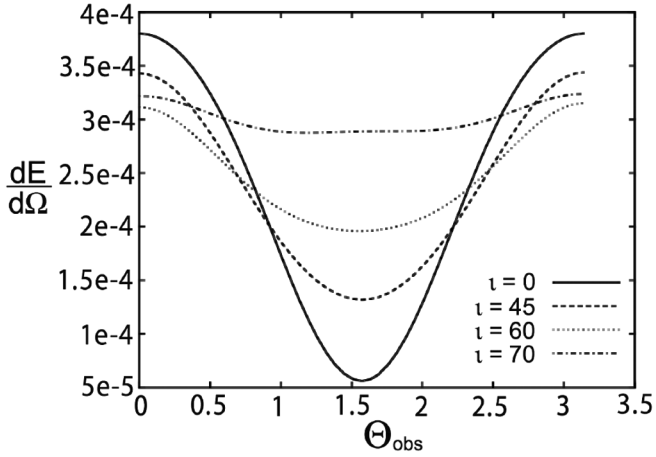

FIG. 11. Angular radiation pattern—energy radiated per unit solid angle as a function of the colatitude of the observer, $\Theta_{\rm obs}$, for orbits with $p = 5M$, $e = 0.4$, $a = 0.9M$ and a sequence of inclinations, as labeled.

$e = 0.1$, 0.4. The flux has been computed using the pure quadrupole waveforms (16). It is clear from Fig. 10 that the averaged flux converges over time, and this convergence is more rapid for the lower eccentricity orbit. In all subsequent flux calculations, we took $T = 10^5 M$ (which corresponds to ~6 days for $M = 10^6 M_\odot$).

In Fig. 11 we show the angular distribution of the gravitational radiation from an EMRI orbit of given p and e, but for several different orbital inclinations, ι. This picture is more or less typical of the majority of orbits. The variation of the energy flux with the sky position of the observer is indicative of beaming. This is strongest for equatorial orbits and reduces as the orbital inclination is increased. Equatorial orbits are restricted to a single plane, while inclined orbits wander through more of the spacetime. This wandering averages out the beaming over the sky. The larger the orbital inclination, the more of the phase space the body explores, the more averaging occurs and the more homogeneous the sky distribution of the energy flux.

In Tables IV and V we show flux data for a series of orbits and black hole spins. We tabulate the flux computed via solution of the Teukolsky equation, and fluxes computed using quadrupole kludge waveforms and Eq. (43). We quote only the quadrupole results since the difference from using either the quadrupole-octupole or Press waveforms is quite small. As we mentioned in Sec. II, Tanaka *et al.* [23], and more recently Gair *et al.* [38] computed approximate fluxes for Schwarzschild orbits based on the quadrupole waveform approximation (16). For a random choice of orbits we have found excellent agreement with their results.

For further comparison, we also tabulate the kludge fluxes that have been used to construct inspirals and inspiral waveforms for scoping out LISA data analysis. The difference between these and our current results is a measure of the inconsistency in the kludged inspiral waveforms. In constructing an inspiral waveform, one set of expressions is used to evolve the orbit (given in [9,10]), and a different prescription (the one described here) is used to generate the waveform. This means that the energy carried by the kludge GWs is not equal to the energy lost by the orbit that is supposedly emitting these GWs. This leads to inaccuracies when the kludge waveforms are used to compute SNRs [20]. In the original prescription for kludge inspirals [9], the phase space trajectories were generated using the leading order post-Newtonian results of Ryan [71], evaluated for relativistic orbital parameters. Ryan's expression for the energy flux is

$$\dot{E} = -\frac{32}{5}\frac{\mu^2}{M^2}\left(\frac{M}{p}\right)^5 (1-e^2)^{3/2} \times \left[f_1(e) - \frac{a}{M}\left(\frac{M}{p}\right)^{3/2} f_2(e)\cos\iota\right], \tag{46}$$

where the e-dependent coefficients are

$$f_1(e) = 1 + \frac{73}{24}e^2 + \frac{37}{96}e^4, \qquad f_2(e) = \frac{73}{12} + \frac{823}{24}e^2 + \frac{949}{32}e^4 + \frac{491}{192}e^6. \tag{47}$$

In a more recent version of the kludge [10], this prescription for the evolution of the orbital parameters was improved. The new expression for $\dot{E}$ is complicated and we do not quote it here, but we also tabulate those results in Tables IV and V, under the heading "GG".

We note that in true black hole spacetimes, energy and angular momentum are lost into the horizon as well as to infinity. The Teukolsky equation provides a prediction for both the flux of radiation at infinity and the flux down the black hole horizon. When using Eqs. (41)–(44), we are only computing the energy and angular momentum carried to infinity in the kludge GWs. This should therefore only be compared to the Teukolsky flux at infinity. The discrepancy between these numbers is then a measure of the error associated with using the kludge waveforms to estimate signal-to-noise ratios for true inspirals. The TB fluxes quoted in the tables are accordingly just the infinity piece of the fluxes. When computing inspirals, which was the purpose for which the GG expressions were derived, the energy and angular momentum lost by the orbit should include the horizon piece of the flux. This should be born in mind when considering the flux tables. However, the relative contribution of the horizon flux is only significant in the extremely strong field regime where both the GG expressions and the kludge fluxes cease to be valid.

In general, we find that the fluxes computed from the kludge waveforms agree less well with Teukolsky results than do the GG fluxes. The kludge fluxes do improve over GG results for some retrograde orbits, and for some orbits with high eccentricity, but these are orbits for which the GG expressions are known to lack some terms. Once the

GG expressions are further improved along the lines discussed in [10], it is likely that the GG fluxes will always be closer to TB results. Typically, the fluxes computed from the kludge waveforms underestimate the actual energy and angular momentum lost by the orbit, and also underestimate the GG fluxes. This suggests that inspiral waveforms that combine the two prescriptions will carry too little energy to infinity for the evolution seen in the orbit (or equivalently, the inspiral will proceed too quickly for the energy being carried by the GWs). In [38], a similar comparison was performed for inspirals into Schwarzschild black holes, and they found that the kludge GWs contained *too much* energy, in contrast to this result. This difference arises primarily because, in that paper, inspirals were evolved using the "Ryan" fluxes, rather than the more up-to-date GG fluxes. The signal-to-noise ratio squared of a monochromatic source contributed when the frequency is in the range $f \rightarrow f + \mathrm{d}f$ is proportional to $\dot{E}\mathrm{d}f/(f^2\dot{f}S_h(f))$. The kludge waveforms get $\dot{f}$ largely correct (otherwise the high overlaps would not be maintained), but the error in $\dot{E}$, arising from an amplitude discrepancy, will lead to an error in SNRs computed using kludge inspiral waveforms. Since $\dot{E}$ is in general an underestimate, the kludge SNRs will probably be underestimates of the true SNRs. The discrepancy in $\dot{E}$ is at most a few tens of percent. A discrepancy of 25% *throughout* the inspiral would lead to an error in the SNR of only 13%. However, the actual error will be much less, since for the majority of the inspiral the kludge $\dot{E}$ is much closer to the true value, and, as we saw earlier, most of the SNR comes from the early inspiral. The kludge waveforms are thus accurate enough to be used for SNR calculations to estimate astrophysical event rates [20], in which the astrophysical uncertainties far outweigh the waveform uncertainties. However, we must emphasize that amplitude discrepancies of this sort do not limit the applicability of the kludge waveforms for data analysis, provided the overlaps with true waveforms are high. If the kludge waveforms were used for parameter extraction, such discrepancies would lead to an error in the distance estimate only. In practice, we are likely to use kludge waveforms for *detection* rather than source characterization, and for that the waveform amplitude is irrelevant.

Table V tabulates data for "parabolic" orbits, $e = 1$. The GW emission from such orbits is important for the capture problem, i.e., the mechanism by which compact objects are put onto EMRI orbits. Gravitational radiation from such orbits has been studied in the past using the Teukolsky formalism [40,61], but tabulated data has only appeared in a recent time-domain analysis by Martel [42]. Those results are claimed to be accurate at the level of $\lesssim 1\%$, and therefore can be treated as exact for our purposes. Table V contains the relevant data together with our kludge results. For a periastron $r_p \sim 5M$ the error in using the kludge fluxes is $\sim$30% and rapidly decays (grows) as we move to larger (smaller) periapse. In this Table we have also included some data for nonequatorial parabolic orbits, but for this class of orbits there are as yet no available TB results. Our experience with bound generic orbits suggests it is likely these data will have accuracies of the same order as the equatorial orbits with a similar periastron. In Fig. 12, we plot ΔE as a function of r_p and L_z (left and right panels, respectively) for parabolic orbits with $a/M = 0$, 0.99 and $\iota = 0°, 60°, 120°, 180°$. All curves are computed using the quadrupole waveform flux (16) and are terminated at the point where the orbit plunges. Figure 12 has astrophysical significance as it displays (within the accuracy of the present calculation) the amount of energy lost in a single parabolic (or $e \approx 1$) encounter with a SMBH, for a variety of inclinations and for a range of periastra that are appropriate to the capture problem [8,72]. This energy loss data can be used to estimate the capture rate of compact objects by a single massive black hole.

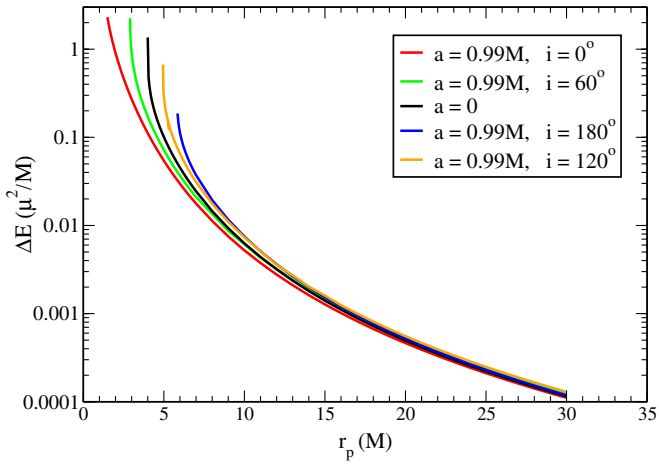

FIG. 12 (color online). Total radiated energy for Kerr parabolic orbits; as function of periastron.

We note that it is clear from Table V that the GG results perform quite poorly for parabolic orbits. This is because the GG results are built on a small eccentricity expansion, which is no longer valid when $e = 1$. At present the kludge fluxes are closer to TB results than the GG fluxes where comparisons can be made, and most likely are better approximations for the other orbits as well. The performance of the GG fluxes for highly eccentric orbits is now being improved, and it is likely that the next generation prescription will be able to approximate TB fluxes accurately for orbits of all eccentricities.

V. INCLUSION OF CONSERVATIVE CORRECTIONS

In the preceding sections, we have shown that kludge waveforms do very well at reproducing the GW emission from geodesic orbits, and, if coupled to an accurate prescription for the radiation fluxes, can very accurately reproduce the GW emission from inspirals. However, the

radiation fluxes are not the whole story, as they represent only the dissipative piece of the self-force. In true inspirals, the self-force also has a conservative component. This does not lead to evolution of the orbital parameters and hence cannot be determined from the flux of energy, angular momentum and Carter constant, but does lead to a change in the phasing of the gravitational waveform. There has been some debate recently about the importance of including the conservative pieces of the self-force when constructing templates for EMRI source detection [73,74]. It is quite possible that these corrections will be needed for detection, at least for some range of source parameters; these terms will certainly be needed for parameter determination. We aim to demonstrate here how easily conservative terms can be included in the kludge waveform prescription.

The conservative part of the self-force will include an oscillatory component, which averages to zero, and a secular piece that leads to accumulation of a phase error over time. The net effect of the secular piece is that, for a given set of orbital parameters (p, e and ι), the average frequencies of the motion in the r, θ and ϕ directions will differ from the expected values for a Kerr geodesic. The conservative self-force might also affect the harmonic structure of the GWs, but the dominant contribution will come from orbital dephasing. In the spirit of the kludge, we will now try to account for this part of the effect.

The effect of the conservative self-force can be characterized by the changes in the r, θ and ϕ frequencies, averaged over many orbits. We denote these frequency changes by $\delta\Omega_r$, $\delta\Omega_\theta$ and $\delta\Omega_\phi$. Conservative effects can then be included in the kludge orbital determination simply by amending the evolution equations for the angular variables ψ, χ and ϕ given earlier (Eqs. (8), (9), and (1c) respectively):

$$\begin{aligned}\left(\frac{d\psi}{dt}\right) &= \left(\frac{d\psi}{dt}\right)_{\rm geo} + 2\pi\delta\Omega_r,\\ \left(\frac{d\chi}{dt}\right) &= \left(\frac{d\chi}{dt}\right)_{\rm geo} + 2\pi\delta\Omega_\theta,\\ \left(\frac{d\phi}{dt}\right) &= \left(\frac{d\phi}{dt}\right)_{\rm geo} + 2\pi\delta\Omega_\phi.\end{aligned} \tag{48}$$

The subscript "geo" denotes expressions for the phase derivatives in geodesic orbits given earlier. In general, the frequency shifts will depend on the orbital parameters, and for an inspiralling source we assume that these are evaluated for the instantaneous orbital parameters, as discussed in Sec. II C 1.

To evaluate these frequency shifts in the framework of black hole perturbation theory requires self-force calculations [26] which are not yet fully developed, but should be on the timescale of a few years. Once the self-force corrections are known, it should be possible to use them to compute the effective frequency shifts in the framework we use here, i.e., objects moving on geodesics of the Kerr spacetime, the parameters of which evolve with time. In the meantime, conservative corrections are already known in the post-Newtonian framework up to 3.5PN order [75]. These can be used to compute leading order conservative corrections to include in the kludge. We outline here a general method for such a calculation, illustrated by the simplest case of a 1PN conservative correction to circular orbits in the Schwarzschild spacetime. The generalization to 3.5PN corrections for arbitrary orbits in Kerr will be presented in a future paper.

The greatest difficulty in such a computation is to identify coordinates between the post-Newtonian and perturbative formalism. The former calculations tend to be carried out in harmonic coordinates while the natural coordinate system to use for the latter are black hole centered coordinates, like the Boyer-Lindquist coordinate system. The best approach is to use asymptotic observables, specifically the orbital frequency, perihelion precession frequency, orbital plane precession frequency and their first time derivatives, to identify coordinates between the two formalisms and find the missing conservative pieces. The power of this approach is that it corrects the kludge in a physically meaningful way; however, this comes at the cost of an effective $O(\eta)$ redefinition of the orbital parameters, where $\eta = \mu/M$. For extreme mass ratios, $\eta < 10^{-4}$, this is less than the expected error in parameter determination [31].

The post-Newtonian model has two particles moving on orbits (expanded to the stated post-Newtonian order) and evolving via post-Newtonian radiation-reaction expressions. These orbits include conservative corrections to geodesic motion. For the case of circular orbits in Schwarzschild we find at 1PN and with mass ratio corrections at linear order only that the orbital frequency and its time derivative are given by [76]

$$\frac{d\phi}{dt} \equiv \Omega = \left(\frac{M}{R}\right)^{3/2}\frac{1}{M}\left(1 + \frac{\eta}{2} - \left(\frac{M}{R}\right)\left(\frac{3}{2} + \frac{7}{4}\eta\right)\right) \tag{49}$$

$$\frac{d\Omega}{dt} = \frac{96}{5}\frac{\eta}{M^2}\left(\frac{M}{R}\right)^{11/2}\left(1 + \frac{3}{2}\eta - \left(\frac{M}{R}\right)\left(\frac{2591}{336} + \frac{13571}{672}\eta\right)\right). \tag{50}$$

In the above, we use M to denote the mass of the primary (not the total mass as is conventional in the post-Newtonian approach), and R to denote the post-Newtonian orbital semimajor axis. In the kludge, the orbit is a geodesic of the Kerr spacetime, and the orbit is evolved according to the prescription in [10]. For circular equatorial orbits in Schwarzschild we have (at 1PN order)

$$\Omega = \frac{1}{r}\left(\frac{M}{r}\right)^{1/2} \tag{51}$$

$$\frac{dr}{dt} = -\frac{64}{5}\frac{\mu}{M}\left(\frac{M}{r}\right)^3\left(1 - \frac{743}{336}\left(\frac{M}{r}\right)\right) \tag{52}$$

$$\Rightarrow \frac{d\Omega}{dt} = \frac{96}{5}\frac{\eta}{M^2}\left(\frac{M}{r}\right)^{11/2}\left(1 - \frac{743}{336}\left(\frac{M}{r}\right) + O\left(v^{3/2}\right)\right). \tag{53}$$

Here, r denotes the Schwarzschild radial coordinate of the orbit. If we write

$$r = R\left(1 + \left(\frac{M}{R}\right)b_0 + \cdots + \eta c_0 + \eta\left(\frac{M}{R}\right)c_1 + \cdots\right), \tag{54}$$

and substitute into expression (51) or (53), keeping corrections at 1PN order and linear in the mass ratio, we can compare to Eqs. (49) or (50) and solve for b_0, c_0 and c_1. The comparison between (49) and (51) gives a different result for c_0 and c_1 than the comparison between (50) and (53), since the kludge prescription ignores conservative effects. We therefore write

$$\begin{aligned}\Omega &= \frac{1}{r}\left(\frac{M}{r}\right)^{1/2} + \delta\Omega \\ &= \frac{1}{r}\left(\frac{M}{r}\right)^{1/2} + \eta\left(\frac{M}{r}\right)^{3/2}\frac{1}{M}\left(d_0 + d_1\left(\frac{M}{r}\right)\right),\end{aligned} \tag{55}$$

and solve simultaneously for b_0, c_0, c_1, d_0 and d_1 [bearing in mind that (52) not (53) is the fundamental quantity to examine for computing inspiral in the kludge]. We find that the required parameters are

$$\begin{aligned} b_0 = 1, \qquad c_0 = -\frac{1}{4}, \qquad c_1 = \frac{845}{448}, \\ d_0 = \frac{1}{8}, \qquad d_1 = \frac{1975}{896}. \end{aligned} \tag{56}$$

We note that the correction to Ω scales as $R^{-3/2}$, compared to the scaling of $\dot{\Omega}$, which is $R^{-11/2}$. In the weak-field, $R \to \infty$, the conservative correction will be much more significant than the radiative correction. This is in keeping with what Pound *et al.* [74] found for a particle moving under an electromagnetic self-force.

Extension to generic orbits is straightforward. In that case, we have two extra observables, the perihelion precession frequency and the rate of precession of the orbital plane, and two extra coordinate dependent orbital parameters, the eccentricity and orbital inclination. Identifying the rate of change of the orbital frequency, the perihelion precession frequency and the orbital plane precession frequency between the post-Newtonian and kludge approaches gives us a relation between the two sets of coordinates. Comparing the values of the frequencies then tells us which $\delta\Omega_\phi$, $\delta\Omega_\theta$ and $\delta\Omega_r$ must be added into the kludge. In all of this we have chosen implicitly to identify the two masses, M and μ, and the spin, a, between the post-Newtonian and kludge models. To our minds, it makes more sense to hold these parameters fixed between the two models, at the cost of modifying the definitions of the orbital elements p, e, ι.

Once self-force data is available, it will be possible to obtain a consistent solution for the conservative correction in Boyer-Lindquist like coordinates by using fits to the self-force results. In using Eq. (52), we have implicitly assumed the relationship between energy/angular momentum and the radial coordinate is unchanged by the self-force. However, in self-force calculations, the energy and angular momentum of circular orbits at a given radius do change as a result of conservative effects. This is merely a manifestation of the $O(\eta)$ redefinition of r implicit in this approach that we mentioned earlier. When comparing to self-force calculations, it will be preferable to include this redefinition of energy as well as the conservative corrections to Ω so that r maintains its meaning. Ultimately, both approaches are equivalent. Another way to obtain d_0 and d_1 for Eq. (55) is by expanding $d\Omega/dt$ as a function of Ω in both the PN and kludge approaches. Matching various orders in this expansion gives d_0 and d_1 directly without having to simultaneously solve for the coordinate transformation. The function $d\Omega/dt(\Omega)$ is a GW observable, so this approach ensures that the kludge will have the correct leading order form for this observable. However, this is a series truncated at a given PN order, so it will be important to assess how significant the omitted terms can be. It is likely that using the present kludge, augmented with conservative corrections up to 3.5PN order computed as outlined above, will do well enough at reproducing the phasing of true inspiral waveforms. As discussed in [74], it is likely that the conservative terms will be most important in the weak-field regime, where the post-Newtonian results are valid. In the regime where the post-Newtonian corrections cease to be valid, the contribution of conservative corrections to the phase evolution may be much less critical. This will be investigated in future work. If the PN expansion is not sufficient, the kludge can be augmented using fits to the results of self-force calculations as described.

VI. CONCLUDING DISCUSSION

In this paper we have provided a simple, "easy-to-use", prescription for approximating the gravitational waveforms generated by test-bodies inspiralling into Kerr black holes. These kludge waveforms are constructed by combining familiar flat-spacetime wave equations with a true geodesic trajectory in the Kerr spacetime. Despite its formal inconsistency this hybrid approximation results in remarkably accurate waveforms, which we have established by comparison to rigorous Teukolsky-based perturbative waveforms. We find an impressive overlap between

the kludge and TB waveforms for particles on geodesic orbits (i.e., ignoring radiation-reaction). This overlap is $>95\%$ over a significant portion of the relevant orbital parameter space. Significant degradation (overlap reduced to $\sim 50\%$) occurs for strong field orbits around rapidly spinning black holes. For such cases, the contribution of the radiation backscattered from the background spacetime is sizable; this effect is not included in the present formulation of the kludge waveforms. As a rough (but reliable) rule of thumb, we have found that kludge waveforms work well for Kerr orbits with periaspe distance $r_p \gtrsim 5M$, irrespective of the black hole spin.

We have experimented with three different types of kludge waveforms generated using three different solutions of the flat-spacetime gravitational wave-equation: quadrupole, quadrupole-octupole and ''Press'' waveforms [36]. The latter choice includes contributions from all multipole moments of the orbiting body. We have concluded that for all practical purposes the quadrupole-octupole waveforms are the optimal choice, nearly as accurate as the Press waveforms while much quicker and easier to generate.

Within the adiabatic approximation, we have applied our method to calculate full inspiral kludge waveforms taking into account orbital evolution. This realistic scenario requires an additional kludge for describing the orbital evolution itself. Our earlier work [9,10] provides such a scheme: exact geodesic orbital dynamics coupled with approximate PN-based expressions for the fluxes. The resulting waveforms still have very high overlaps with available Teukolsky-based inspirals for circular-inclined orbits. The overlap is $\gtrsim 75\%$ even when the inspiral terminates in the strong ield region. This result indicates the kludge will be a very useful tool for generating inspiral waveforms. However, as yet Teukolsky-based inspirals are available only for circular-inclined orbits. Only when comparisons for generic inspiral orbits are possible will we be able to firmly identify the range of applicability of these kludge waveforms.

We have also used the kludge waveforms to estimate the fluxes of energy and angular momentum carried away in GWs from geodesic orbits. We have found that such kludge fluxes in general are not as accurate for evolving inspirals as the post-Newtonian based expressions described in [10]. The kludge fluxes do provide us with an estimate of the error in using kludge waveforms for SNR calculations, and our results suggest the kludge waveforms will tend to underestimate the true SNRs if anything.

The area where these kludge waveforms will find most use is in the development of EMRI data analysis for LISA. The combination of accuracy and simplicity of generation has already made these waveforms invaluable tools for the study of data analysis issues. It seems quite plausible that the waveforms may also play a role in the final search of the LISA data. One use could be for estimation of the waveform parameters as the first stage in a hierarchical search. The high faithfulness of these waveforms suggest that they may be able to set fairly tight bounds on the parameters of the emitting system. This will be extremely useful input for the second stage of the search where the system parameters will be refined using more accurate waveforms. However, as we discussed before, the kludge waveforms at present do not include some important physical features that we expect in true inspirals. Only when accurate Teukolsky or self-force based waveforms are available for generic inspiral orbits will we be able to fully quantify the range of validity and level of accuracy of the kludge waveforms.

Time-frequency searches [77–79] could also be used to detect EMRIs in the first stage of a hierarchical search. These can typically detect EMRI events at about half the distance of the semicoherent search [20], without the use of templates. A template with overlap of $\sim 50\%$ with the true signal can detect that signal at about half the distance of the correct template. The NK waveforms can easily achieve overlaps of $\sim 50\%$ through most of parameter space, particularly given the $2-3$ week integration times needed for the semicoherent approach. It is clear therefore that a first stage semicoherent search using kludge waveforms would have a greater reach than time-frequency methods, and would put tighter constraints on the parameters. However, this would come at a much greater computational cost. The final LISA search will undoubtedly employ both methods at various stages in the analysis.

A further possible application of kludge waveforms is to the study of non-Kerr EMRIs. It is hoped that LISA observations will allow ''spacetime-mapping'' of black holes [16,80], and thereby test the no-hair theorem. To carry out such tests quantitatively will require waveform templates, which incorporate the deviation from Kerr in the spacetime structure as a set of suitable parameters (e.g., multipole moments [16]). The development of rigorous non-Kerr EMRI waveforms is a very difficult task, since generic spacetimes lack some symmetries that allowed the formulation of the Teukolsky framework for the Kerr spacetime. One way to make progress is to construct kludged waveforms in non-Kerr spacetimes along the lines outlined in this paper. Our results for the Kerr spacetime suggest that such kludged waveforms may well be sufficiently accurate for qualitative, and even quantitative studies of non-Kerr EMRIs. All that is required is the integration of geodesic equations in the non-Kerr spacetime and thus kludge waveforms provide a computationally quick and easy tool to study ''bumpy'' and ''quasi-Kerr'' spacetime mapping [17,18].

The kludged waveforms/inspirals presented in this and a companion paper [10] could be considered as ''second generation'', an improvement of the original simple version of quadrupole waveforms [30] and inspirals [9]. Certainly, there is space for further improvement. The inclusion of conservative self-force effects on the inspiral

is an obvious next step, and we have already discussed here how this can be achieved by calculating the relevant orbital frequency shifts for circular Schwarzschild orbits. We can also further improve waveform generation by including the backscattering effect arising from the propagation of the GWs in a curved spacetime.

In summary, given the present level of performance of our kludge waveforms and inspirals and their prospects of improvement, we feel that they should remain valuable tools for LISA source modelling for the coming years.

ACKNOWLEDGMENTS

We thank Kip Thorne for initially pointing us to the paper by Press, Steve Drasco for providing Teukolsky-based waveforms from generic orbits and B. S. Sathyaprakash for useful discussions. The work of J. R. G. was supported in part by NASA grants NAG5-12834 and NAG5-10707 and by St. Catharine's College, Cambridge. K. G. acknowledges support from PPARC Grant No. PPA/G/S/2002/00038. Work of S. B. was partially supported by PPARC Grant No. PP/B500731. Work of H. F. was supported in parts by NASA grants NAG5-12834, NNG04GK98G and by NSF grants PHY-0099568 and PHY-0601459. The work of S. A. H. was supported by NASA Grants NAG5-12906 and NNG05G105G, NSF Grant No. PHY-0244424 and CAREER grant No. PHY-0449884. S. A. H. also gratefully acknowledges support from MIT's Class of 1956 Career Development Fund.

APPENDIX A: TABLES

TABLE I. Numerical data for overlaps between TB and kludge waveforms–equatorial-eccentric Kerr orbits. Data is not shown with WD confusion noise for the ten orbits in the very strong field regime. In this regime, none of the kludge waveforms reproduce the TB waveforms very well, and this is compounded when the dominant harmonics are suppressed by white dwarf confusion noise. The overlaps are uniformly poor and uninformative, so we do not include them.

p/M[a]	e[b]	ι[c] (deg)	a/M[d]	Θ[e] (deg)	overlap(+)[f]			overlap with WD (+)[g]			duration(M)[h]
					Quad	Quad-Oct	Press	Quad	Quad-Oct	Press	
1.7	0.1	0	0.99	90	0.84	0.772	0.741				2000
1.7	0.3	0	0.99	90	0.76	0.557	0.500				700
1.9	0.5	0	0.99	90	0.544	0.570	0.547				700
1.9	0.5	0	0.99	90	0.523	0.484	0.445				2000
2.11	0.7	0	0.99	45	0.562	0.566	0.562				700
2.2	0.7	0	0.99	90	0.526	0.496	0.458				700
2.5	0.1	0	0.99	90	0.906	0.853	0.827				2000
2.5	0.5	0	0.99	90	0.671	0.665	0.651				700
3.5	0.4	0	0.99	90	0.588	0.524	0.507				2000
3.5	0.4	0	0.99	45	0.624	0.598	0.593				5000
5.1	0.5	0	0.5	90	0.856	0.962	0.967	0.856	0.961	0.968	700
5.5	0.5	0	0.5	90	0.864	0.964	0.973	0.862	0.962	0.973	2000
6.0	0.4	0	0.5	90	0.871	0.970	0.980	0.864	0.967	0.979	2000
6.0	0.5	0	0.5	90	0.858	0.966	0.974	0.855	0.963	0.973	2000
6.5	0.5	0	0.5	90	0.870	0.970	0.979	0.864	0.968	0.978	2000
6.5	0.5	0	0.5	45	0.937	0.987	0.990	0.932	0.986	0.990	8000
10.0	0.3	180	0.99	90	0.864	0.961	0.966	0.806	0.943	0.954	8000
10.0	0.3	180	0.99	45	0.922	0.971	0.969	0.883	0.957	0.956	8000
10.4	0.5	180	0.99	0	0.998	0.998	0.999	0.997	0.999	0.998	2000
10.5	0.5	180	0.99	90	0.878	0.975	0.982	0.856	0.968	0.978	2000
15.0	0.4	0	0.5	90	0.824	0.963	0.968	0.60	0.878	0.881	8000
15.0	0.4	0	0.99	90	0.824	0.961	0.963	0.603	0.874	0.860	8000

[a]semilatus rectum
[b]eccentricity
[c]inclination angle
[d]spin
[e]observation point, $\phi = 0$ always
[f]overlap between "+" polarization of TB waveform with quadrupole ("Quad"), quadrupole-octupole ("Quad-Oct") and Press (Press) kludge waveforms
[g]overlap between "×" polarizations
[h]waveform duration

TABLE II. Numerical data for overlaps between TB and kludge waveforms—inclined-circular Kerr orbits.

p/M	e	ι (deg)	a/M	Θ (deg)	overlap(+)			overlap(×)			overlap with WD (×)			duration(M)
					Quad	Quad-Oct	Press	Quad	Quad-Oct	Press	Quad	Quad-Oct	Press	
5.0	0	30	0.5	45	0.944	0.984	0.990	0.946	0.984	0.990	0.945	0.984	0.990	3000
5.0	0	30	0.5	90	0.899	0.974	0.984	0.891	0.971	0.984	0.89	0.969	0.983	3000
5.0	0	30	0.99	45	0.929	0.969	0.975	0.93	0.969	0.975	0.927	0.967	0.974	3000
5.0	0	30	0.99	90	0.904	0.958	0.964	0.9	0.957	0.966	0.895	0.954	0.965	3000
5.05	0	60	0.5	45	0.924	0.967	0.973	0.922	0.969	0.977	0.922	0.968	0.976	3000
5.05	0	60	0.5	90	0.91	0.955	0.961	0.911	0.963	0.973	0.907	0.961	0.972	3000
5.0	0	60	0.99	45	0.857	0.912	0.917	0.86	0.917	0.925	0.857	0.913	0.921	3000
5.0	0	60	0.99	90	0.854	0.882	0.888	0.87	0.912	0.925	0.862	0.907	0.922	3000
10.0	0	30	0.5	45	0.93	0.989	0.995	0.936	0.99	0.994	0.751	0.957	0.975	8000
10.0	0	30	0.5	90	0.89	0.981	0.990	0.901	0.981	0.990	0.63	0.93	0.969	7000
10.0	0	30	0.99	45	0.92	0.98	0.986	0.93	0.98	0.986	0.674	0.92	0.946	8000
10.0	0	30	0.99	90	0.884	0.974	0.982	0.915	0.975	0.983	0.371	0.892	0.963	7000
10.0	0	45	0.7	45	0.932	0.980	0.981	0.936	0.983	0.987	0.75	0.935	0.953	8000
10.0	0	45	0.7	90	0.922	0.972	0.972	0.92	0.98	0.987	0.68	0.929	0.969	8000
10.0	0	60	0.5	45	0.914	0.981	0.987	0.912	0.982	0.990	0.691	0.937	0.969	8000
10.0	0	60	0.5	90	0.945	0.98	0.981	0.932	0.981	0.986	0.732	0.925	0.948	7000
10.0	0	60	0.99	45	0.873	0.953	0.958	0.875	0.957	0.965	0.611	0.875	0.906	8000
10.0	0	60	0.99	90	0.923	0.941	0.937	0.915	0.959	0.965	0.675	0.86	0.893	7000
20.0	0	30	0.5	45	0.934	0.987	0.982	0.938	0.989	0.989	0.957	0.987	0.902	50000
20.0	0	30	0.5	90	0.889	0.970	0.922	0.893	0.974	0.962	0.92	0.984	0.900	30000
20.0	0	30	0.99	45	0.93	0.98	0.951	0.94	0.988	0.992	0.951	0.987	0.977	50000
20.0	0	30	0.99	90	0.895	0.968	0.907	0.914	0.979	0.988	0.933	0.979	0.951	30000
20.0	0	60	0.5	45	0.92	0.975	0.966	0.916	0.981	0.995	0.952	0.958	0.990	50000
20.0	0	60	0.5	90	0.95	0.973	0.958	0.934	0.976	0.972	0.95	0.967	0.957	30000
20.0	0	60	0.99	45	0.895	0.963	0.962	0.892	0.967	0.973	0.934	0.951	0.896	50000
20.0	0	60	0.99	90	0.954	0.96	0.938	0.937	0.972	0.978	0.963	0.946	0.943	30000

TABLE III. Numerical data for overlaps between TB and kludge waveforms—generic Kerr orbits.

p/M	e	ι (deg)	a/M	Θ (deg)	overlap(+)			overlap(×)			overlap with WD (×)			duration(M)
					Quad	Quad-Oct	Press	Quad	Quad-Oct	Press	Quad	Quad-Oct	Press	
6.0	0.1	20.1364	0.9	90	0.912	0.982	0.993	0.91	0.984	0.996	0.894	0.98	0.995	15000
6.0	0.1	20.1364	0.9	60	0.935	0.988	0.996	0.939	0.99	0.997	0.929	0.989	0.997	15000
6.0	0.1	20.1364	0.9	30	0.972	0.995	0.998	0.972	0.995	0.998	0.968	0.995	0.998	15000
6.0	0.5	20.103	0.9	90	0.89	0.967	0.973	0.89	0.972	0.980	0.875	0.968	0.979	15000
6.0	0.5	20.103	0.9	60	0.916	0.975	0.980	0.912	0.978	0.982	0.913	0.976	0.981	15000
6.0	0.5	20.103	0.9	30	0.958	0.985	0.985	0.959	0.985	0.986	0.955	0.984	0.985	15000
6.0	0.1	60.1461	0.9	90	0.951	0.989	0.993	0.941	0.988	0.995	0.933	0.987	0.995	10000
6.0	0.1	60.1461	0.9	60	0.958	0.989	0.994	0.95	0.988	0.995	0.946	0.987	0.996	10000
6.0	0.1	60.1461	0.9	30	0.943	0.986	0.996	0.942	0.987	0.996	0.941	0.986	0.996	10000
6.0	0.5	60.1108	0.9	90	0.934	0.975	0.980	0.919	0.974	0.982	0.912	0.971	0.981	15000
6.0	0.5	60.1108	0.9	60	0.939	0.974	0.982	0.927	0.972	0.984	0.924	0.97	0.984	15000
6.0	0.5	60.1108	0.9	30	0.917	0.971	0.978	0.916	0.971	0.979	0.915	0.971	0.979	15000
6.0	0.7	60.0755	0.9	90	0.926	0.966	0.970	0.911	0.967	0.974	0.906	0.966	0.975	20000
6.0	0.7	60.0755	0.9	60	0.928	0.967	0.971	0.919	0.966	0.974	0.916	0.966	0.974	20000
6.0	0.7	60.0755	0.9	30	0.897	0.963	0.966	0.897	0.963	0.967	0.897	0.963	0.968	20000
12.0	0.1	119.9586	0.9	90	0.916	0.987	0.994	0.911	0.988	0.998	0.627	0.922	0.985	15000
12.0	0.1	119.9586	0.9	60	0.926	0.988	0.991	0.92	0.989	0.998	0.634	0.926	0.985	15000
12.0	0.1	119.9586	0.9	30	0.9	0.983	0.994	0.899	0.986	0.994	0.577	0.91	0.956	15000
12.0	0.5	119.9686	0.9	90	0.938	0.988	0.992	0.934	0.988	0.995	0.889	0.979	0.993	15000
12.0	0.5	119.9686	0.9	60	0.942	0.988	0.993	0.936	0.987	0.994	0.889	0.977	0.991	15000

TABLE III. (*Continued*)

p/M	e	ι (deg)	a/M	Θ (deg)	overlap(+)			overlap(×)			overlap with WD (×)			duration(M)
					Quad	Quad-Oct	Press	Quad	Quad-Oct	Press	Quad	Quad-Oct	Press	
12.0	0.5	119.9686	0.9	30	0.924	0.984	0.993	0.924	0.986	0.994	0.862	0.971	0.988	15000
12.0	0.7	119.9786	0.9	90	0.935	0.986	0.992	0.933	0.987	0.993	0.904	0.981	0.991	25000
12.0	0.7	119.9786	0.9	60	0.940	0.987	0.992	0.934	0.985	0.992	0.904	0.978	0.990	25000
12.0	0.7	119.9786	0.9	30	0.926	0.983	0.992	0.924	0.983	0.990	0.884	0.973	0.986	25000
12.0	0.3	139.9597	0.9	90	0.9	0.985	0.992	0.891	0.984	0.996	0.751	0.955	0.991	15000
12.0	0.3	139.9597	0.9	60	0.938	0.991	0.994	0.931	0.99	0.997	0.827	0.972	0.993	15000
12.0	0.3	139.9597	0.9	30	0.948	0.992	0.994	0.949	0.993	0.998	0.859	0.979	0.994	15000
12.0	0.1	159.9728	0.9	90	0.836	0.973	0.992	0.838	0.974	0.993	0.494	0.887	0.968	15000
12.0	0.1	159.9728	0.9	60	0.881	0.984	0.995	0.889	0.987	0.998	0.549	0.926	0.990	15000
12.0	0.1	159.9728	0.9	30	0.947	0.994	0.997	0.947	0.995	0.997	0.726	0.96	0.968	15000
12.0	0.5	159.9793	0.9	90	0.876	0.976	0.991	0.877	0.977	0.995	0.808	0.961	0.993	15000
12.0	0.5	159.9793	0.9	60	0.912	0.985	0.994	0.919	0.988	0.996	0.862	0.977	0.994	15000
12.0	0.5	159.9793	0.9	30	0.961	0.994	0.996	0.962	0.995	0.998	0.932	0.991	0.996	15000

TABLE IV. A comparison of the approximate fluxes computed from the kludge quadrupole waveforms (16) described in this paper to accurate Teukolsky-based fluxes for circular (top section), equatorial (middle section) and generic (bottom section) orbits. The energy fluxes are expressed in units of μ^2/M, and the angular momentum fluxes in units of μ^2/M^2. The subscripts "TB", GG and quad denote fluxes computed from Teukolsky-based waveforms, from the kludge flux expressions in [10] and the approximate quadrupole fluxes, respectively.

a/M	p/M	e	ι	$\langle \dot{E} \rangle_{\rm TB}$	$\langle \dot{E} \rangle_{\rm GG}$	$\langle \dot{E} \rangle_{\rm quad}$	$\langle \dot{L}_z \rangle_{\rm TB}$	$\langle \dot{L}_z \rangle_{\rm GG}$	$\langle \dot{L}_z \rangle_{\rm quad}$
0.95	100	0	60.	$-6.219e-10$	$-6.219e-10$	$-6.381e-10$	$-3.118e-7$	$-3.122e-7$	$-3.204e-7$
0.5	5	0.3	0.	$-2.604e-3$	$-2.17e-3$	$-2.08e-3$	$-2.48e-2$	$-2.00e-2$	$-2.03e-2$
0.5	5	0.4	0.	$-3.530e-3$	$-2.37e-3$	$-2.57e-3$	$-2.98e-2$	$-1.94e-2$	$-2.24e-2$
0.5	6	0.3	0.	$-8.883e-4$	$-8.45e-4$	$-7.99e-4$	$-1.13e-2$	$-1.03e-2$	$-1.03e-2$
0.5	6	0.4	0.	$-1.033e-3$	$-9.17e-4$	$-8.77e-4$	$-1.18e-2$	$-1.00e-2$	$-1.03e-2$
0.5	6	0.5	0.	$-1.196e-3$	$-9.51e-4$	$-9.50e-4$	$-1.23e-2$	$-9.41e-3$	$-1.00e-2$
0.9	12.152	0.3731	0.	$-2.357e-5$	$-2.352e-5$	$-2.47e-5$	$8.1351e-4$	$-7.99e-4$	$-8.46e-4$
0.99	2	0.1	0.	$-4.723e-2$	$-3.94e-2$	$-3.34e-2$	-0.178	-0.120	-0.126
0.99	2	0.3	0.	$-5.634e-2$	$-5.084e-2$	$-3.62e-2$	-0.190	$2.39e-3$	-0.125
0.99	2	0.4	0.	$-6.429e-2$	$-4.11e-2$	$-3.90e-2$	-0.201	$9.55e-2$	-0.125
0.99	3	0.1	0.	$-1.124e-2$	$-1.096e-2$	$-9.33e-3$	$-6.83e-2$	$-6.29e-2$	$-5.69e-2$
0.99	3	0.3	0.	$-1.315e-2$	$-1.434e-2$	$-9.88e-3$	$-7.10e-2$	$-5.47e-2$	$-5.46e-2$
0.99	11	0.2	180.	$-5.639e-5$	$-5.25e-5$	$-5.36e-5$	$1.81e-3$	$1.71e-3$	$1.73e-3$
0.99	11	0.4	180.	$-8.337e-5$	$-6.12e-5$	$-7.25e-5$	$2.13e-3$	$1.65e-3$	$1.89e-3$
0.99	11	0.5	180.	$-1.049e-4$	$-6.38e-5$	$-8.60e-5$	$2.36e-3$	$1.55e-3$	$1.98e-3$
0.9	6	0.1	40.192 285	$-6.1850e-4$	$-6.196e-4$	$-6.112e-4$	$-7.628e-3$	$-7.534e-3$	$-7.547e-3$
0.9	6	0.3	40.176 668	$-7.2678e-4$	$-7.512e-4$	$-6.744e-5$	$-7.835e-3$	$-7.632e-3$	$-7.359e-3$
0.9	6	0.5	40.145 475	$-8.7445e-4$	$-8.475e-4$	$-7.344e-4$	$-7.8084e-3$	$-7.143e-3$	$-6.686e-3$
0.9	6	0.7	40.098 788	$-8.7037e-4$	$-6.834e-4$	$-6.506e-4$	$-6.488e-3$	$-5.140e-3$	$-4.945e-3$
0.9	6	0.1	80.046 323	$-8.0701e-4$	$-8.007e-4$	$-7.283e-4$	$-3.6182e-3$	$-3.395e-3$	$-3.328e-3$
0.9	6	0.3	80.042 690	$-1.0863e-3$	$-9.879e-4$	$-8.851e-4$	$-4.369e-3$	$-3.659e-3$	$-3.698e-3$
0.9	6	0.5	80.035 363	$-1.6792e-3$	$-1.163e-3$	$-1.167e-3$	$-5.874e-3$	$-3.761e-3$	$-4.321e-3$
0.9	6	0.7	80.024 226	$-2.6923e-3$	$-1.010e-3$	$-1.537e-3$	$-8.251e-3$	$-3.002e-3$	$-5.056e-3$
0.9	12	0.1	99.982 344	$-2.5084e-5$	$-2.511e-5$	$-2.621e-5$	$1.228e-3$	$1.238e-4$	$1.261e-4$
0.9	12	0.3	99.983 766	$-2.9241e-5$	$-2.900e-5$	$-2.963e-5$	$1.143e-4$	$1.150e-4$	$1.143e-4$
0.9	12	0.5	99.986 612	$-3.4405e-5$	$-3.231e-5$	$-3.315e-5$	$9.515e-5$	$9.419e-5$	$8.989e-5$
0.9	12	0.7	99.990 888	$-3.2914e-5$	$-2.749e-5$	$-2.973e-5$	$6.196e-5$	$5.865e-5$	$5.345e-5$
0.9	12	0.1	139.956 153	$-2.8394e-5$	$-2.828e-5$	$-2.883e-5$	$8.406e-4$	$8.389e-4$	$8.530e-4$
0.9	12	0.3	139.959 664	$-3.445e-5$	$-3.265e-5$	$-3.361e-5$	$8.6536e-4$	$8.265e-4$	$8.481e-4$
0.9	12	0.5	139.966 702	$-4.3778e-5$	$-3.657e-5$	$-3.963e-5$	$8.674e-4$	$7.506e-4$	$7.964e-4$
0.9	12	0.7	139.977 303	$-4.623e-5$	$-3.153e-5$	$-3.818e-5$	$7.287e-4$	$5.343e-4$	$6.121e-4$

TABLE V. As in Table IV, but for parabolic orbits.

a/M	p/M	e	ι	$\Delta E_{\rm TB}$	$\Delta E_{\rm GG}$	$\Delta E_{\rm quad}$	$\Delta Lz_{\rm TB}$	$\Delta Lz_{\rm GG}$	$\Delta Lz_{\rm quad}$
0	8.001	1	0	-2.28	-0.157	-0.976	-19.1	-0.664	-8.45
0	10	1	0	$-1.47e-1$	$-6.62e-2$	-0.101	-1.90	-0.971	-1.36
0	14	1	0	$-2.93e-2$	$-1.87e-2$	$-2.44e-2$	-0.631	-0.450	-0.540
0	20	1	0	$-6.78e-3$	$-5.08e-3$	$-6.26e-3$	-0.250	-0.206	-0.235
0	50	1	0	$-2.199e-4$	$-1.97e-4$	$-2.21e-4$	$-3.26e-2$	$-3.05e-2$	$-3.28e-2$
0.9	15	1	0	$\cdots$	$-0.011\,15$	$-0.014\,41$	$\cdots$	-0.3190	-0.3646
0.9	15	1	60	$\cdots$	$-0.012\,84$	$-0.015\,66$	$\cdots$	-0.1999	-0.2204
0.9	15	1	120	$\cdots$	$-0.016\,33$	$-0.020\,57$	$\cdots$	0.1882	0.2126
0.9	15	1	180	$\cdots$	$-0.018\,15$	$-0.025\,27$	$\cdots$	0.4656	0.6035
0.99	15	1	0	$\cdots$	$-0.010\,84$	$-0.014\,03$	$\cdots$	-0.3129	-0.3567
0.99	15	1	60	$\cdots$	$-0.012\,69$	$-0.015\,31$	$\cdots$	-0.2007	-0.2184
0.99	15	1	120	$\cdots$	$-0.016\,53$	$-0.020\,64$	$\cdots$	0.1878	0.2097
0.99	15	1	180	$\cdots$	$-0.018\,53$	$-0.026\,26$	$\cdots$	0.4744	0.6250

[1] K. Danzman *et al.*, LISAã Laser Interferometer Space Antenna, Pre-Phase A Report, Max-Planck-Institute fur Quantenoptic, Report No. MPQ 233, 1998 (unpublished).

[2] D. Merritt and L. Ferrarese, in *The Central Kpc of Starbursts and AGN*, edited by J. H. Knapen *et al.* (A.S.P., San Francisco, 2001), p. 335; see also ASP Conf. Ser. **249**, 335 (2001).

[3] M. Sarzi, *et al.*, Astrophys. J. **567**, 237 (2002).

[4] M. J. Rees, *Proceedings of S. Chandrasekhar Memorial Conference on Black Holes and Relativistic Stars* (University of Chicago Press, Chicago, 1998);

[5] S. Sigurdsson, Classical Quantum Gravity **14**, 1425 (1997).

[6] M. J. Rees, Classical Quantum Gravity **14**, 1411 (1997).

[7] S. Sigurdsson and M. J. Rees, Mon. Not. R. Astron. Soc. **284**, 318 (1997).

[8] M. Freitag, Classical Quantum Gravity **18**, 4033 (2001); Astrophys. J. Lett. **583**, L21 (2003).

[9] K. Glampedakis, S. A. Hughes, and D. Kennefick, Phys. Rev. D **66**, 064005 (2002).

[10] J. R. Gair and K. Glampedakis, Phys. Rev. D **73**, 064037 (2006).

[11] K. Glampedakis, Classical Quantum Gravity **22**, S605 (2005).

[12] L. Barack and C. Cutler, Phys. Rev. D **70**, 122002 (2004).

[13] L. J. Rubbo, K. Holley-Bockelmann, and L. S. Finn, astro-ph/0602445.

[14] S. A. Hughes, Phys. Rev. D **61**, 084004 (2000); **64**, 064004 (2001).

[15] K. Glampedakis and D. Kennefick, Phys. Rev. D **66**, 044002 (2002).

[16] F. D. Ryan, Phys. Rev. D **52**, 5707 (1995).

[17] N. A. Collins and S. A. Hughes, Phys. Rev. D **69**, 124022 (2004).

[18] K. Glampedakis and S. Babak, Classical Quantum Gravity **23**, 4167 (2006).

[19] G. Nelemans, L. R. Yungelson, and S. F. Portegies Zwart, Astron. Astrophys. **375**, 890 (2001).

[20] J. R. Gair, L. Barack, T. Creighton, C. Cutler, S. L. Larson, E. S. Phinney, and M. Vallisneri, Classical Quantum Gravity **21**, S1595 (2004).

[21] S. A. Teukolsky, Astrophys. J. **185**, 635 (1973).

[22] C. Cutler, D. Kennefick, and E. Poisson, Phys. Rev. D **50**, 3816 (1994).

[23] T. Tanaka, M. Shibata, M. Sasaki, H. Tagoshi, and T. Nakamura, Prog. Theor. Phys. **90**, 65 (1993).

[24] S. Drasco and S. A. Hughes, Phys. Rev. D **73**, 024027 (2006).

[25] Y. Mino, M. Sasaki, M. Shibata, H. Tagoshi, and T. Tanaka, Prog. Theor. Phys. Suppl. **128**, 1 (1998).

[26] E. Poisson, Living Rev. Relativity **7**, 6 (2004), http://www.livingreviews.org/lrr-2004-6.

[27] E. Poisson, Phys. Rev. D **47**, 1497 (1993); E. Poisson and M. Sasaki, Phys. Rev. D **51**, 5753 (1995).

[28] J. Levin, R. O'Reilly, and E. J. Copeland, Phys. Rev. D **62**, 024023 (2000).

[29] E. Poisson, Phys. Rev. D **48**, 1860 (1993).

[30] Material on a variety of LISA and EMRI topics can be found at the following www address: http://www.tapir.caltech.edu/list/index.html.

[31] L. Barack and C. Cutler, Phys. Rev. D **69**, 082005 (2004).

[32] C. Moreno-Garrido, E. Mediavilla, and J. Buitrago, Mon. Not. R. Astron. Soc. **274**, 115 (1995).

[33] T. Creighton, J. R. Gair, S. A. Hughes, and M. Vallisneri (unpublished).

[34] C. W. Misner, K. S. Thorne, and J. A. Wheeler, *Gravitation* (Freeman, San Francisco, 1973).

[35] J. D. Bekenstein, Astrophys. J. **183**, 657 (1973).

[36] W. H. Press, Phys. Rev. D **15**, 965 (1977).

[37] S. A. Hughes, Phys. Rev. D **64**, 064004 (2001).

[38] J. R. Gair, D. J. Kennefick, and S. L. Larson, Phys. Rev. D **72**, 084009 (2005).

[39] S. A. Teukolsky and W. H. Press, Astrophys. J. **193**, 443 (1974).

[40] S. L. Detweiler, Astrophys. J. **225**, 687 (1978).

[41] M. Sasaki and T. Nakamura, Prog. Theor. Phys. **67**, 1788 (1982).

[42] E. Poisson, Phys. Rev. D **70**, 084044 (2004); K. Martel, Phys. Rev. D **69**, 044025 (2004); K. Martel and E. Poisson, Phys. Rev. D **66**, 084001 (2002).

[43] R. Lopez-Aleman, G. Khanna, and J. Pullin, Classical Quantum Gravity **20**, 3259 (2003).

[44] E. Possion, Classical Quantum Gravity **21**, R153 (2004).
[45] L. Kidder, Phys. Rev. D **52**, 821 (1995).
[46] A. Buonanno, Y. Chen, and M. Vallisneri, Phys. Rev. D **67**, 104025 (2003).
[47] Y. Pan, A. Buonanno, Y. Chen, and M. Vallisneri, Phys. Rev. D **69**, 104017 (2004).
[48] L. Blanchet and A. Buonanno, gr-qc/0605140.
[49] T. Damour, Phys. Rev. D **64**, 124013 (2001).
[50] A. Buonanno and T. Damour, Phys. Rev. D **59**, 084006 (1999); **62**, 064015 (2000); T. Damour, P. Jaranowski, and G. Shafer, Phys. Rev. D **62**, 084011 (2000).
[51] C. Koenigsdoerffer and A. Gopakumar, Phys. Rev. D **73**, 124012 (2006).
[52] T. Damour, A. Gopakumar, and B. Iyer, Phys. Rev. D **70**, 064028 (2004).
[53] R. Memmesheimer, A. Gopakumar, and G. Schaefer, Phys. Rev. D **70**, 104011 (2004).
[54] P. C. Peter and J. Mathews, Phys. Rev. **131**, 435 (1963); P. C. Peter, Phys. Rev. **136**, B1224 (1964).
[55] R. Ruffini and M. Sasaki, Prog. Theor. Phys. **66**, 1627 (1981).
[56] M. Sasaki, Prog. Theor. Phys. **69**, 815 (1983).
[57] J. M. Bardeen, W. H. Press, and S. A. Teukolsky, Astrophys. J. **178**, 347 (1972).
[58] S. Chandrasekhar, *The Mathematical Theory of Black Holes* (Oxford Univ. Press, New York, 1983).
[59] J. Binney and S. Tremaine, *Galactic Dynamics* (Princeton University Press, Princeton, NJ, 1987), Chap. 3.
[60] L. Blanchet, T. Damour, and B. Iyer, Phys. Rev. D **51**, 5360 (1995).
[61] Y. Kojima and T. Nakamura, Prog. Theor. Phys. **72**, 494 (1984).
[62] C. Cutler and E. Flanagan, Phys. Rev. D **49**, 2658 (1994).
[63] R. Balasubramanian, B. S. Sathyaprakash, and S. Dhurandhar, Phys. Rev. D **53**, 3033 (1996).
[64] T. Damour, B. R. Iyer, and B. Sathyaprakash, Phys. Rev. D **57**, 885 (1998).
[65] http://www.srl.caltech.edu/shane/sensitivity/MakeCurve.html; S. L. Larson, W. A. Hiscock, and R. W. Hellings, Phys. Rev. D **62**, 062001 (2000).
[66] S. Drasco and S. A. Hughes, Phys. Rev. D **69**, 044015 (2004).
[67] D. B. Percival and A. T. Walden, *Spectral Analysis for Physical Applications* (Cambridge University Press, Cambridge, England, 1993).
[68] R. A. Isaacson, Phys. Rev. **166**, 1263 (1968).
[69] R. A. Isaacson, Phys. Rev. **166**, 1272 (1968).
[70] K. S. Thorne, Rev. Mod. Phys. **52**, 299 (1980).
[71] F. D. Ryan, Phys. Rev. D **53**, 3064 (1996).
[72] J. R. Gair, D. J. Kennefick, and S. L. Larson, Astrophys. J. **639**, 999 (2006).
[73] S. Drasco, E. E. Flanagan, and S. A. Hughes, Classical Quantum Gravity **22**, S801 (2005).
[74] A. Pound, E. Poisson, and B. G. Nickel, Phys. Rev. D **72**, 124001 (2005).
[75] L. Blanchet, Living Rev. Relativity **5**, 3 (2002), http://www.livingreviews.org/lrr-2002-3.
[76] W. Junker and G. Schaefer, Mon. Not. R. Astron. Soc. **254**, 146 (1992).
[77] L. Wen and J. R. Gair, Classical Quantum Gravity **22**, S445 (2005).
[78] J. R. Gair and L. Wen, Classical Quantum Gravity **22**, S1359 (2005).
[79] J. R. Gair and G. Jones, gr-qc/0610046.
[80] C. Cutler and K. Thorne, gr-qc/0204090.